Exploration of R_2XM_2 (R=Sc, Y, Ti, Zr, Hf, rare earth; X=main group element; M=transition metal, Si, Ge): Structural motifs, the novel compound Gd_2AlGe_2 and analysis of the U_3Si_2 and Zr_3Al_2 structure types

by

Sean William McWhorter

A thesis submitted to the graduate faculty

in partial fulfillment of the requirements for the degree of

MASTER OF SCIENCE

Major: Inorganic Chemistry

Program of Study Committee:
Gordon J. Miller (Major Professor)
John D. Corbett
Vitalij Pecharsky

Iowa State University

Ames, Iowa

2003

Graduate College

Iowa State University

This is to certify that the master's thesis of

Sean William McWhorter

has met the thesis requirements of Iowa State University

Committee Member

Committee Member

Major Professor

For the Major Program

Table of Contents

Abstract

In the process of exploring and understanding the influence of crystal structure on the system of compounds with the composition $Gd_5(Si_xGe_{1-x})_4$ several new compounds were synthesized with different crystal structures, but similar structural features. In $Gd_5(Si_xGe_{1-x})_4$, the main feature of interest is the magnetocaloric effect (MCE), which allows the material to be useful in magnetic refrigeration applications. The MCE is based on the magnetic interactions of the Gd atoms in the crystal structure, which varies with x (the amount of Si in the compound). The crystal structure of $Gd_5(Si_xGe_{1-x})_4$ can be thought of as being formed from two 3^2434 nets of Gd atoms, with additional Gd atoms in the cubic voids and Si/Ge atoms in the trigonal prismatic voids. Attempts were made to substitute nonmagnetic atoms for magnetic Gd using In, Mg and Al. Gd_2MgGe_2 and Gd_2InGe_2 both possess the same 3^2434 nets of Gd atoms as $Gd_5(Si_xGe_{1-x})_4$, but these nets are connected differently, forming the Mo_2FeB_2 crystal structure. A search of the literature revealed that compounds with the composition R_2XM_2 (R=Sc, Y, Ti, Zr, Hf, rare earth; X=main group element; M=transition metal, Si, Ge) crystallize in one of four crystal structures: the Mo_2FeB_2, Zr_3Al_2, Mn_2AlB_2 and W_2CoB_2 crystal structures. These crystal structures are described, and the relationships between them are highlighted.

Gd_2AlGe_2 forms an entirely new crystal structure, and the details of its synthesis and characterization are given. Electronic structure calculations are performed to understand the nature of bonding in this compound and how electrons can be accounted for.

A series of electronic structure calculations were performed on models with the U_3Si_2 and Zr_3Al_2 structures, using Zr and Al as the building blocks. The starting point for these models was the U_3Si_2 structure, and models were created to simulate the transition from the

idealized U_3Si_2 structure to the distorted Zr_3Al_2 structure. Analysis of the band structures of the models has shown that the transition from the U_3Si_2 structure to the Zr_3Al_2 structure lifts degeneracies along the $\Gamma \rightarrow Z$ direction, indicating a Peierls-type mechanism for the displacement occurring in the positions of the Zr atoms.

Research Motivation and Literature Review

Introduction

There is currently a great deal of interest in developing materials to be used for magnetic refrigeration in order to replace the current gas compression/expansion technology. Current gas compression technology is approaching its limits for increasing energy efficiency, and also utilizes chlorofluorocarbons (CFC's), which have been shown to have a negative impact on the environment. Magnetic refrigeration materials offer improvements in both efficiency and environmental impact. A successful proof-of-principle magnetic refrigerator has been constructed by Zimm et al. [1], and makes use of Gd metal as the refrigerant material.

Gd is used as the refrigerant material due to the magnetocaloric effect (MCE). The MCE is intrinsic to all magnetic materials, and arises from the coupling of the magnetic sublattice of the material with an applied external field. This coupling results in a change in the magnetic entropy of the solid, similar to the way the isothermal compression/expansion of an ideal gas affects the entropy of the gas. Formally, the MCE is characterized by an adiabatic temperature change, ΔT_{ad}, and an isothermal magnetic entropy change, ΔS_M:

$$\Delta T_{ad}(T,\Delta H) = -\int_{H_1}^{H_2}\left(\frac{T}{C(T,H)}\right)_H\left(\frac{dM(T,H)}{dT}\right)_H dH$$

$$\Delta S_M(T,\Delta H) = \int_{H_1}^{H_2}\left(\frac{dM(T,H)}{dT}\right)_H dH$$

Qualitatively, the MCE arises in magnetic materials as an increase in the temperature of the solid as an external field is applied (magnetic entropy decreases) [2]. The Curie temperature

of Gd is 303 K, and the MCE of Gd has been studied, yielding a MCE of 3 K/T in low magnetic fields and ~2 K/T in higher fields [3].

Research in this area has continued, searching for materials that order magnetically between 250 K and 310 K that have superior properties to those of pure Gd. In a systematic study of intermetallic compounds containing rare earth elements, it was discovered that a giant MCE existed in the alloys $Gd_5(Si_xGe_{1-x})_4$, with $x \geq 0.5$. The Curie temperature of the alloy can be tuned from 335 K to ~20 K by increasing the concentration of Ge. The MCE for these alloys is called "giant" due to the size of ΔS_M, which is at least 2 times larger than that of Gd at room temperature, and 2 to 10 times larger than the ΔS_M values of the best previously known magnetocaloric materials e.g., at low to intermediate temperatures [4]. The giant MCE in $Gd_5(Si_xGe_{1-x})_4$ appears to have a long lifetime with respect to cycling, a crucial feature for use in magnetic refrigeration.

The origin of the giant MCE in $Gd_5(Si_xGe_{1-x})_4$ seems to lie in the fact that there is a crystallographic phase transition that occurs along with the expected magnetic phase transition, such that it can be described as a magnetic order-disorder and crystallographic order-order transformation [5].

Numerous magnetic studies of $Gd_5(Si_xGe_{1-x})_4$ have shown that the types of magnetic ordering for a given composition depend upon temperature, magnetic field and the crystal structure of that particular alloy [6, 7, 8]. The structure of each alloy is based upon $^{\infty}{}_2[Gd_5(Si_xGe_{1-x})_4]$ slabs held together by Si/Ge dimers. Each slab is formed from two 3^2434 nets of Gd atoms, with additional Gd atoms in the cubic voids and Si/Ge atoms in the trigonal prismatic voids (see Figure 1.1). The variations in magnetic properties are attributed to the

interactions between 3^2434 nets of Gd atoms, namely the presence of magnetic Gd atoms and an intervening layer of non-magnetic Si/Ge atoms and also the presence of an intervening layer of Si/Ge atoms between the slabs.

In order to better understand the complex magnetic interactions present in $Gd_5(Si_xGe_{1-x})_4$, attempts to substitute nonmagnetic atoms for Gd atoms were made. In the course of these experiments, two new compounds have been isolated and characterized: Gd_2MgGe_2 and Gd_2AlGe_2 [9, 10]. Gd_2MgGe_2 is an ordered, ternary variant of the U_3Si_2 structure type, containing the same 3^2434 nets of Gd as $Gd_5(Si_xGe_{1-x})_4$, but lacking the bonding between the slabs that is present in $Gd_5(Si_xGe_{1-x})_4$ (see Figure 1.2). The Mg atoms in Gd_2MgGe_2 occupy the cubic voids in the 3^2434 net of Gd, allowing the relationships between composition and magnetic properties to be studied. In contrast, Gd_2AlGe_2 forms an entirely new structure type, with no resemblance to the structure type of either $Gd_5(Si_xGe_{1-x})_4$ or Gd_2MgGe_2 (see Figure 1.3).

In this thesis, three main topics will be covered. In this first chapter, a general review of the structure types of compounds with the composition RE_2XM_2 (RE= Sc, Y, Ti, Zr, Hf, rare earth; X= main group element; M= transition metal, Si, Ge) will be studied. In the second chapter, a new compound and structure type, Gd_2AlGe_2, will be introduced and discussed. In the third, an examination of the U_3Si_2 and Zr_3Al_2 structure types will be performed and the relationship of the electronic structures between them will be analyzed.

Literature Review

In the RE_2XM_2 system, all known compounds form one of 5 structure types. The two most frequent structure types are both tetragonal, and are the U_3Si_2 and Zr_3Al_2 structure types. Less common are two different orthorhombic structures that also form: the W_2CoB_2 and Mn_2AlB_2 structure types. Finally, a new structure type in the 2-1-2 phase has been recently discovered: the monoclinic Gd_2AlGe_2 structure, which has only one representative in the RE_2XM_2 system so far.

A comprehensive list of compounds found in the literature that crystallize in one of these structure types and has the composition R_2XM_2 is listed in Tables 1.1-1.4, along with the lattice constants and typical synthetic conditions for each compound.

The U_3Si_2 structure is tetragonal, with the space group *P4/mbm*, and *Z*=2. The structure is built of U trigonal and square prisms stacked along the *c* axis, with the Si atoms filling the voids of the trigonal prisms. These structural motifs can be described as derived from the AlB_2 and CsCl structures, resulting in fragments consisting of Si_2U and U_2, with the net composition adding up to U_3Si_2. Alternately, one can think of the U_3Si_2 structure as being built out of two eclipsed 3^2434 nets composed of U atoms, with U atoms occupying the cubic voids and Si atoms in the voids formed by the eclipsed U triangles. In the R_2XM_2 system, the U_3Si_2 structure type occurs as the so-called "Mo_2FeB_2" structure type, which is a ternary, ordered version of the U_3Si_2 structure. In the Mo_2FeB_2 structure, the Mo atoms form the network of trigonal and square prisms, but Fe occupies the void in the Mo cube. The trigonal prisms then have a composition of MoB_2. This can be generalized for the rest of the compounds in the R_2XM_2 system, such that any compound that forms the Mo_2FeB_2 structure type can be visualized as consisting of two elementary motifs: the RX network of square prisms and the RM_2 network of trigonal prisms. Examples of the Mo_2FeB_2 structure type are

RE_2LiSi_2 (RE=Y, Nd) [11], RE_2MgNi_2 (RE=Y, La-Sm, Gd-Tm) [12] and RE_2InAu_2 (RE=Y, La-Sm, Gd-Yb) [13] (see Table 1.1).

The Zr_3Al_2 structure is a superstructure of the U_3Si_2 structure type, and is related by a group-subgroup relationship where *P4₂/mnm* (Zr_3Al_2-type) is a *klassengleiche* subgroup of *P4/mbm* (U_3Si_2-type). The *c* axis of Zr_3Al_2 is doubled with respect to U_3Si_2, resulting in *Z*=4, rather than 2. This doubling of the *c* axis is due to a distortion that occurs in the network of Zr atoms that form the vertices of the trigonal and squares prisms (see Figure 1.4). Instead of stacking neatly along the *c* axis, as the U atoms do in U_3Si_2, the Zr atoms instead form zigzag chains. Also, the Al pairs formed by side sharing trigonal prisms are moved away from the mirror planes. Alternately, as in the U_3Si_2 structure, the Zr_3Al_2 structure can also be thought of as a pair of eclipsed 3^2434 nets composed of Zr atoms, with Zr atoms in the cubic voids and Al atoms in the trigonal voids. Unlike the U_3Si_2 structure, the 3^2434 nets are not regular, but are instead slightly distorted in the plane of the net. As a result, the squares of Zr atoms are not regular, and this in turn generates the 4_2 screw axis in the structure. Examples of RE_2XM_2 that form the Zr_3Al_2 structure are RE_2InAu_2 (RE=Sc, Zr, Hf, Tm, Lu)[13], RE_2SnAu_2 (RE=Sc, Y, Dy-Tm, Lu)[14] and A_2InNi_2 (A=Ti, Zr, Hf)[15] (see Table 1.2).

The W_2CoB_2 structure is orthorhombic, with space group *Immm* and *Z*=2. The crystal structure of W_2CoB_2 is complex, but can be thought of as building off a W skeleton (see Figure 1.5). The W atoms form a puckered 6^3 net, while the Co and B atoms form planar nets with the composition $[CoB_2]$. In the $[CoB_2]$ nets, the Co is bonded to four B atoms and the B atoms are three-bonded to 2 Co and another B, forming B-B dimers. Some examples of compounds from the RE_2XM_2 system that form the W_2CoB_2 structure are RE_2SnNi_2, where RE= Ce, Nd, Gd, Tb, Dy [16, 17, 18] (see Table 1.3).

The Mn_2AlB_2 structure is a fourth type of structure that is formed by compounds with the composition RE_2XM_2. Some examples of compounds with this structure type are RE_2InNi_2, where RE=Y, Sm, Gd-Tm, Lu [19] (see Table 1.4). Like the W_2CoB_2 structure, the structure of Mn_2AlB_2 is also orthorhombic, but it has the space group *Cmmm*, with *Z*=2. The Mn_2AlB_2 structure can be thought of as consisting of 2 components: an infinite 2D net of edge-sharing trigonal prisms composed of B atoms with a quasi-infinite array of Al and Mn atoms separating the B nets (see Figure 1.6). The Al and Mn atoms are arranged in a psuedo-CsCl network, with each Al atom surrounded by 8 Mn atoms. As you look down the *b* axis, the Al atoms are shifted ½ a lattice translation along the *c* and *b* axes, resulting in a staggering of the psuedo-CsCl slabs of AlMn. The same effect also occurs with the layers of B atoms as well. As a simple approximation, one can think of this structure as two staggered slabs of either AlMn separated by similarly staggered slabs of B as you travel down the long (*b*) axis, extending infinitely in the *ac* plane.

The fifth crystal structure type known to form in the RE_2XM_2 system is the Gd_2AlGe_2 structure type, which has space group *C2/c* and *Z*=4. Currently, Gd_2AlGe_2 is the only known example of this structure type, which is characterized by a 3 dimensional network in which the Al is four-bonded to Ge atoms in a slightly distorted "sawhorse" geometry while the Ge atoms are planar three-bonded to two Al atoms and one other Ge atom. The Gd atoms are packed in space such that loosely puckered 6^3 nets of Gd atoms are centered on Al atoms. The synthesis and properties of Gd_2AlGe_2 will be discussed in the next chapter more thoroughly.

References

[1] C. B. Zimm, A. J. DeGregoria, in: H. S. Kwok, D. T. Show, H. J. Naughton (Eds.), *Proceedings of the 6th International Conference Superconduct. Applic.*, Buffalo, NY, September 15-17, AIP, New York, 1993, 471.

[2] K. A. Gschneidner, Jr., et al. *Phys. Rev. B.* **2001**, 64, 144406/1.

[3] V. K. Pecharsky, D. C. Jiles, et al. *J. Appl. Phys.* **2002**, 91, 8894.

[4] V. K. Pecharsky, K. A. Gschneidner, Jr. *Appl. Phys. Lett.* **1997**, *70*, 3299.

[5] V. K. Pecharsky, K. A. Gschneidner, Jr. *Mat. Sci and Eng.* **2000**, A287, 301.

[6] V. K. Pecharsky, K. A. Gschneidner, Jr. *J. Alloys Comp.* **1997**, 260, 98.

[7] L. Morellon, P. A. Algarabel, et al. *Phys. Rev. B.* **1998**, 58, R14721.

[8] W. Choe, V. K. Pecharsky, G. J. Miller, K. A. Gschneidner Jr., et al. *Phys. Rev. Lett.* **2000**, 84, 4617.

[9] W. Choe, G. J. Miller, E. M. Levin. *J. Alloys Comp.* **2001**, 329, 121.

[10] W. Choe, S. W. McWhorter, G. J. Miller. *Z. Anorg. Allg. Chem.* **2002**, 628, 1575.

[11] G. Steinberg, H. U. Schuster, et al. *Z. Naturforsch. B: Anorg. Chem., Org. Chem.* **1979**, 34B, 1237.

[12] R. Pöttgen, et al. *Z. Anorg. Allg. Chem.* **2000**, 626, 1733.

[13] F. Hulliger, et al. *J. Alloys Comp.* **1996,** 232, 160.

[14] R. Pöttgen, et al. *Z. Naturforsch.* **1994**, 49b, 1309.

[15] R. Pöttgen, et al. *Z. Naturforsch.* **1996,** 51b, 1248.

[16] B. Chevalier, et al. *J. Alloys Comp.* **1995,** 218, 90.

[17] B. Chevalier, et al. *Physica B.* **1996,** 226, 283.

[18] B. Chevalier, et al. *J. Alloys Comp.* **1997,** 262, 114.

[19] V. I. Zaremba, et al. *Neo. Mat.* **1988,** 24, 409.

[20] V. K. Pecharsky, et al. *J. Alloys Comp.* **2002**, 138, 126.

[21] R. Pöttgen, et al. *Z. Naturforsch.* **2000**, 55b, 155.

[22] A. O. Sampaio, et al. *J. Less-Comm. Metals.* **1968**, 14, 472.

[23] R. Pöttgen, et al. *J. Solid State Chem.* **2000**, 150, 139.

[24] R. Pöttgen, et al. *Z. Anorg. Allg. Chem.* **2001**, 627, 1283.

[25] Peron, M. N., et al. *J. Alloys Comp.* **1993**, 201, 203.

[26] R. Pöttgen, et al. *Z. Anorg. Allg. Chem.* **1996**, 622, 355.

[27] V. I. Zaremba, et al. *Neo. Mat.* **1990**, 26, 94.

[28] L. C. J. Pereira, et al. *J. Solid State Chem.* **1997**, 134, 138.

[29] V. I. Zaremba, et al. *Z. Kristallogr. New Cryst. Struct.* **1997**, 212, 291.

[30] F. Hulliger, et al. *J. Alloys Comp.* **1995**, 221, L11.

[31] M. Giovanni, et al. *J. Alloys Comp.* **1998**, 280, 26.

[32] F. Hulliger, et al. *J. Alloys Comp.* **1994**, 215, 267.

[33] F. Hulliger, et al. *J. Alloys Comp.* **1995,** 217, 164.

[34] B. Chevalier, et al. *J. Alloys Comp.* **1993,** 191, L1.

[35] R. Pöttgen, et al. *Z. Naturforsch.* **1994**, 49b, 1525.

[36] M. L. Fornasini, et al. *Z. Kristallogr. New Cryst. Struct.* **2001**, 216, 23.

[37] R. Pöttgen, et al. *J. Solid State Chem.* **1997**,128, 289.

[38] R. Pöttgen, et al.. *Z. Anorg. Allg. Chem.* **1998**, 624, 251.

[39] M. L. Fornasini, et al. *Z. Kristallogr. New Cryst. Struct.* **2001**, 216, 24.

Table 1.1 Compounds with U_3Si_2/Mo_2FeB_2 Structure

Compound	*a* (Å)	*c* (Å)	Synthesis Conditions	Reference
Y_2LiSi_2	7.105	4.414	Li_2YSi in Ta under Ar @ 700 °C, anneal 6 h @ 700 °C	[11]
Nd_2LiSi_2	7.37	4.242	Li_2NdSi in Ta heat to 1030 °C, anneal 1 d @ 670 °C	[11]
Y_2MgNi_2	7.404(1)	3.723(1)	Y pre-melted, anneal @ 1500 K, anneal @ 900 K for 2 h	[12]
La_2MgNi_2	7.654(1)	3.926(1)	La pre-melted, heat to 1500 K, anneal @ 900 K for 2 h	[12]
Ce_2MgNi_2	7.596(1)	3.7671(9)	Ce pre-melted, heat to 1500 K, anneal @ 900 K for 2 h	[12]
Pr_2MgNi_2	7.549(1)	3.841(1)	Pr pre-melted, heat to 1500 K, anneal @ 900 K for 2 h	[12]
Nd_2MgNi_2	7.533(1)	3.818(1)	Nd pre-melted, heat to 1500 K, anneal @ 900 K for 2 h	[12]
Sm_2MgNi_2	7.4602(9)	3.7934(8)	Sm pre-melted, heat to 1500 K, anneal @ 900 K for 2 h	[12]
Gd_2MgNi_2	7.438(1)	3.753(1)	Gd pre-melted, heat to 1500 K, anneal @ 900 K for 2 h	[12]
Tb_2MgNi_2	7.404(1)	3.7266(8)	Tb pre-melt, heat to 1500 K, anneal @ 900 K for 2 h	[12]
Dy_2MgNi_2	7.390(1)	3.699(1)	Dy pre-melt, heat to 1500 K, anneal @ 900 K for 2 h	[12]
Ho_2MgNi_2	7.378(2)	3.679(2)	Ho pre-melted, heat to 1500 K, anneal @ 900 K for 2 h	[12]
Er_2MgNi_2	7.3407(4)	3.6682(6)	Er pre-melted, heat to 1500 K, anneal @ 900 K for 2 h	[12]
Tm_2MgNi_2	7.3439(8)	3.6467(8)	Tm pre-melted, heat to 1500 K, anneal @ 900 K for 2 h	[12]
Ce_2MgCu_2	7.8741(9)	3.8723(7)	Ce pre-melted, heat to 1500 K, anneal @ 900 K for 2 h	[21]
Gd_2MgGe_2	7.291(1)	4.2826(8)	Mg_2Ge+Ge+Gd in Ta @ 1373 K, cool to 938 K, quench	[9]
Ce_2MgPd_2	7.7714(8)	4.0003(7)	Ce pre-melted, heat to 1500 K, anneal @ 900 K for 2 h	[21]
U_2AlCo_2	7.091	3.461	found in investigation of U-Al-Co system	[22]
Ce_2CdNi_2	7.5567(8)	3.7514(6)	Ce pre-melted, heat to 1500 K, anneal @ 900 K for 2 h	[23]
Ce_2CdPd_2	7.7790(6)	3.9328(6)	Ce pre-melted, heat to 1500 K, anneal @ 900 K for 2 h	[21]
Ce_2CdPt_2	7.7990(7)	3.8997(7)	Ce pre-melted, heat to 1500 K, anneal @ 900 K for 2 h	[21]
La_2CdAu_2	8.092(1)	4.0027(9)	1500-1100-1500 K cycling, anneal @ 900 K 2h	[24]
Ce_2CdAu_2	8.0493(7)	3.9336(6)	1500-1100-1500 K cycling, anneal @ 900 K 2h	[21]
Pr_2CdAu_2	8.0067(8)	3.910(1)	1500-1100-1500 K cycling, anneal @ 900 K 2h	[24]
Nd_2CdAu_2	7.972(2)	3.885(1)	1500-1100-1500 K cycling, anneal @ 900 K 2h	[24]
Sm_2CdAu_2	7.914(2)	3.827(2)	1500-1100-1500 K cycling, anneal @ 900 K 2h	[24]
Zr_2InCo_2	7.2054(7)	3.3159(4)	Zr, Co pre-melted, arc-melted, anneal @ 1070 K 40 d	[15]
U_2InCo_2	7.366(4)	3.4320(16)	arc-melted at stoichiometry under Ar	[25]
Np_2InCo_2	7.3224(11)	3.5149(11)	arc-melted at stoichiometry under Ar	[25]
Sc_2InNi_2	7.1679(1)	3.33154(8)	arc-melted 3x, annealed @ 1070 K for 10 days in silica	[26]
La_2InNi_2	7.611(3)	3.918(2)	arc-melted, anneal 1070, 870, 670 K for 400, 600, 800 h	[27]
Ce_2InNi_2	7.499(2)	3.751(2)	arc-melted, anneal 1070, 870, 670 K for 400, 600, 800 h	[27]
Pr_2InNi_2	7.526(2)	3.817(1)	arc-melted, anneal 1070, 870, 670 K for 400, 600, 800 h	[27]
Nd_2InNi_2	7.514(2)	3.757(2)	arc-melted, anneal 1070, 870, 670 K for 400, 600, 800 h	[27]
U_2InNi_2	7.374(2)	3.572(1)	arc-melted at stoichiometry under Ar	[25]
Np_2InNi_2	7.3646(16)	3.590(1)	arc-melted at stoichiometry under Ar	[25]
Pu_2InNi_2	7.336(3)	3.690(2)	Pu pre-melted, stoichiometric ratio arc-melted	[28]
Y_2InCu_2	7.470(2)	3.765(2)	arc-melted under Ar, annealed @ 870 K for 600 h	[27]
La_2InCu_2	7.789(2)	3.983(3)	arc-melted under Ar, annealed @ 870 K for 600 h	[27]
Ce_2InCu_2	7.728(1)	3.916(2)	arc-melted under Ar, annealed @ 870 K for 600 h	[27]
Pr_2InCu_2	7.678(1)	3.893(1)	arc-melted under Ar, annealed @ 870 K for 600 h	[27]

Table 1.1 (continued)

Compound	*a* (Å)	*c* (Å)	Synthesis Conditions	Reference
Nd_2InCu_2	7.638(2)	3.877(1)	arc-melted under Ar, annealed @ 870 K for 600 h	[27]
Sm_2InCu_2	7.571(2)	3.823(1)	arc-melted under Ar, annealed @ 870 K for 600 h	[27]
Gd_2InCu_2	7.528(2)	3.798(2)	arc-melted under Ar, annealed @ 870 K for 600 h	[27]
Tb_2InCu_2	7.487(2)	3.772(2)	arc-melted under Ar, annealed @ 870 K for 600 h	[27]
Dy_2InCu_2	7.466(3)	3.746(2)	arc-melted under Ar, annealed @ 870 K for 600 h	[27]
Ho_2InCu_2	7.441(2)	3.731(2)	arc-melted under Ar, annealed @ 870 K for 600 h	[27]
Er_2InCu_2	7.414(3)	3.723(2)	arc-melted under Ar, annealed @ 870 K for 600 h	[27]
Tm_2InCu_2	7.393(1)	3.696(1)	arc-melted under Ar, annealed @ 870 K for 600 h	[27]
Lu_2InCu_2	7.364(1)	3.682(1)	arc-melted under Ar, annealed @ 870 K for 600 h	[27]
Yb_2InGe_2	7.205(1)	4.294(1)	arc-melted, annealed @ 870 K for 720 h	[29]
La_2InRh_2	7.6362(8)	3.9970(8)	arc-melted under Ar, annealed @ 600-750 °C	[30]
Ce_2InRh2	7.5874(3)	3.7709(3)	arc-melted under Ar, annealed @ 600-750 °C	[30]
Pr_2InRh_2	7.5344(8)	3.9383(8)	arc-melted under Ar, annealed @ 600-750 °C	[30]
Nd_2InRh_2	7.5147(3)	3.9117(3)	arc-melted under Ar, annealed @ 600-750 °C	[30]
Sm_2InRh_2	7.4589(5)	3.8849(6)	arc-melted under Ar, annealed @ 600-750 °C	[30]
U_2InRh_2	7.5530(14)	3.605(6)	arc-melted at stoichiometry under Ar	[25]
Np_2InRh_2	7.5318(17)	3.6541(8)	arc-melted at stoichiometry under Ar	[25]
Pu_2InRh_2	7.451(3)	3.741(2)	Pu pre-melted, stoichiometric ratio arc-melted	[28]
Ce_2InPd_2	7.813(4)	3.916(2)	Ce, Pd arc-melted, In added, arc-melted	[31]
Pr_2InPd_2	7.7804(2)	3.8815(1)	Pr, Pd arc-melted, In added, arc-melted	[31]
Nd_2InPd_2	7.7492(2)	3.8678(2)	Nd, Pd arc-melted, In added, arc-melted	[31]
Sm_2InPd_2	7.7009(5)	3.8085(3)	arc-melted at stoichiometry under Ar	[31]
Gd_2InPd_2	7.6829(3)	3.7617(2)	Gd, Pd arc-melted, In added, arc-melted	[31]
Tb_2InPd_2	7.6636(2)	3.7239(1)	Tb, Pd arc-melted, In added, arc-melted	[31]
Dy_2InPd_2	7.6532(4)	3.6937(2)	Dy, Pd arc-melted, In added, arc-melted	[31]
Ho_2InPd_2	7.6404(3)	3.6713(2)	Ho, Pd arc-melted, In added, arc-melted	[31]
Er_2InPd_2	7.6329(2)	3.6446(1)	Er, Pd arc-melted, In added, arc-melted	[31]
Tm_2InPd_2	7.6225(2)	3.6241(1)	Tm, Pd arc-melted, In added, arc-melted	[31]
Yb_2InPd_2	7.5978(3)	3.6405(2)	elements melted in Ta crucible under Ar	[31]
Lu_2InPd_2	7.6046(2)	3.585(2)	Lu, Pd arc-melted, In added, arc-melted	[31]
Th_2InPd_2	7.627(3)	3.769(3)	arc-melted under Ar	[32]
U_2InPd_2	7.6396(12)	3.7533(11)	arc-melted at stoichiometry under Ar	[25]
Np_2InPd_2	7.6526(12)	3.7987(14)	arc-melted at stoichiometry under Ar	[25]
Pu_2InPd_2	7.657(2)	3.818(1)	Pu pre-melted, stoichiometric ratio arc-melted	[28]
U_2InIr_2	7.596(13)	3.582(5)	arc-melted at stoichiometry under Ar	[25]
Y_2InPt_2	7.6586(4)	3.6768(4)	arc-melted under Ar	[33]
La_2InPt_2	7.8735(4)	3.9433(4)	arc-melted under Ar	[33]
Ce_2InPt_2	7.8038(3)	3.8830(2)	arc-melted under Ar	[33]
Pr_2InPt_2	7.7762(4)	3.8695(4)	arc-melted under Ar	[33]
Nd_2InPt_2	7.7639(3)	3.8331(3)	arc-melted under Ar	[33]
Sm_2InPt_2	7.7108(7)	3.7896(5)	arc-melted under Ar	[33]

Table 1.1 (continued)

Compound	*a* (Å)	*c* (Å)	Synthesis Conditions	Reference
Gd_2InPt_2	7.7009(7)	3.7348(6)	arc-melted under Ar	[33]
Tb_2InPt_2	7.6772(4)	3.7051(4)	arc-melted under Ar	[33]
Dy_2InPt_2	7.6511(6)	3.6767(5)	arc-melted under Ar	[33]
Ho_2InPt_2	7.6545(6)	3.6506(6)	arc-melted under Ar	[33]
Th_2InPt_2	7.659(2)	3.618(1)	arc-melted under Ar	[33]
U_2InPt_2	7.687(3)	3.701(4)	arc-melted at stoichiometry under Ar	[25]
Np_2InPt_2	7.6879(9)	3.7199(11)	arc-melted at stoichiometry under Ar	[25]
Pu_2InPt_2	7.663(4)	3.795(1)	Pu pre-melted, stoichiometric ratio arc-melted	[28]
Y_2InAu_2	7.8367(3)	3.7440(2)	arc-melted under Ar, then "arc-annealed" 15-20 min	[13]
La_2InAu_2	8.0963(6)	3.9998(5)	arc-melted under Ar, then "arc-annealed" 15-20 min	[13]
Ce_2InAu_2	8.0427(4)	3.9459(3)	arc-melted under Ar, then "arc-annealed" 15-20 min	[13]
Pr_2InAu_2	8.0025(4)	3.9200(4)	arc-melted under Ar, then "arc-annealed" 15-20 min	[13]
Nd_2InAu_2	7.9760(4)	3.8863(3)	arc-melted under Ar, then "arc-annealed" 15-20 min	[13]
Sm_2InAu_2	7.9302(4)	3.8282(3)	arc-melted under Ar, then "arc-annealed" 15-20 min	[13]
Gd_2InAu_2	7.8688(6)	3.8113(6)	arc-melted under Ar, then "arc-annealed" 15-20 min	[13]
Tb_2InAu_2	7.8535(6)	3.7658(6)	arc-melted under Ar, then "arc-annealed" 15-20 min	[13]
Dy_2InAu_2	7.8248(6)	3.7525(7)	arc-melted under Ar, then "arc-annealed" 15-20 min	[13]
Ho_2InAu_2	7.8134(3)	3.7195(4)	arc-melted under Ar, then "arc-annealed" 15-20 min	[13]
Er_2InAu_2	7.7886(3)	3.7086(3)	arc-melted under Ar, then "arc-annealed" 15-20 min	[13]
Yb_2InAu_2	7.8303(5)	3.8595(4)	arc-melted under Ar, then "arc-annealed" 15-20 min	[13]
U_2SnFe_2	7.296(1)	3.446(1)	melted 2-1-2 ratio under Ar, anneal @ 800 K for 2 w	[34]
U_2SnCo_2	7.290(5)	3.512(5)	arc-melted at stoichiometry under Ar	[25]
U_2SnNi_2	7.234(6)	3.706(5)	arc-melted at stoichiometry under Ar	[25]
Pu_2SnNi_2	7.272(2)	3.745(1)	Pu pre-melted, stoichiometric ratio arc-melted	[28]
Am_2SnNi_2	7.315(3)	3.765(2)	Am pre-melted, stoichiometric ratio arc-melted	[28]
U_2SnRh_2	7.511(5)	3.635(3)	arc-melted at stoichiometry under Ar	[25]
Pu_2SnPd_2	7.607(2)	3.867(1)	Pu pre-melted, stoichiometric ratio arc-melted	[28]
Am_2SnPd_2	7.603(4)	3.851(3)	Am pre-melted, stoichiometric ratio arc-melted	[28]
U_2SnPt_2	7.678(5)	3.699(2)	arc-melted at stoichiometry under Ar	[25]
Pu_2SnPt_2	7.629(2)	3.806(1)	Pu pre-melted, stoichiometric ratio arc-melted	[28]
Gd_2SnAu_2	7.865(3)	3.838(3)	arc-melted under Ar, annealed @ 800 °C for 2 w	[35]
Tb_2SnAu_2	7.829(3)	3.775(4)	arc-melted under Ar, annealed @ 800 °C for 2 w	[35]
Ce_2PbPd_2	7.915(1)	3.872(2)	pre-melt Ce, heat to 1500 K, anneal @ 900 K for 2 h	[21]
Ce_2PbPt_2	7.9463(7)	3.8150(6)	pre-melt Ce, heat to 1500 K, anneal @ 900 K for 2 h	[21]
Ca_2PbAu_2	8.038(1)	3.8254(4)	induction melted in Ta tube under Ar	[36]
Ce_2PbAu_2	8.1070(7)	3.9485(7)	pre-melt Ce, heat to 1500 K, anneal @ 900 K for 2 h	[21]

Table 1.2 Compounds with Zr_3Al_2 Structure

Compound	*a* (Å)	*c* (Å)	Synthesis Conditions	Reference
Ti_2InNi_2	6.943(2)	6.232(2)	Ti pre-melted, arc-melted, anneal @ 1070 K for 40 d	[15]
Zr_2InNi_2	7.151(1)	6.635(1)	arc-melted, annealed @ 1070 K for 14 days in silica	[37]
Hf_2InNi_2	7.139(1)	6.604(2)	Hf pre-melted, arc-melted, anneal @ 970 K up to 3 w	[38]
Sc_2InCu_2	7.2236(4)	6.8955(7)	arc-melted under Ar, then "arc-annealed" 15-20 min	[13]
Zr_2InCu_2	7.2135(5)	6.8402(8)	arc-melted under Ar, then "arc-annealed" 15-20 min	[13]
Hf_2InCu_2	7.155(1)	6.770(1)	Hf pre-melted, arc-melted, anneal @ 970 K up to 3 w	[38]
Sc_2InPd_2	7.498(2)	6.773(2)	arc-melted under Ar, then "arc-annealed" 15-20 min	[13]
Zr_2InPd_2	7.460(1)	6.861(1)	Zr, Pd melted, arc-melted, anneal @ 1070 K for 40 d	[15]
Hf_2InPd_2	7.426(1)	6.794(2)	Hf pre-melted, arc-melted, anneal @ 970 K up to 3 w	[38]
Sc_2InAu_2	7.5669(6)	6.9563(9)	arc-melted under Ar, then "arc-annealed" 15-20 min	[13]
Zr_2InAu_2	7.5263(5)	7.0504(9)	arc-melted under Ar, then "arc-annealed" 15-20 min	[13]
Tm_2InAu_2	7.7795(4)	7.3437(8)	arc-melted under Ar, then "arc-annealed" 15-20 min	[13]
Lu_2InAu_2	7.755(1)	7.287(1)	arc-melted under Ar, then "arc-annealed" 15-20 min	[13]
Hf_2InAu_2	7.4545(10)	7.054(2)	arc-melted under Ar, then "arc-annealed" 15-20 min	[13]
Zr_2SnNi_2	7.032(1)	6.801(1)	arc-melted 3x, anneal @ 1070 K for 14 days in silica	[37]
Hf_2SnNi_2	7.031(1)	6.761(2)	Hf pre-melted, arc-melted, anneal @ 970 K up to 3 w	[38]
Sc_2SnAu_2	7.5282(10)	7.0237(12)	arc-melted under Ar, then "arc-annealed" 15-20 min	[13]
Y_2SnAu_2	7.814(1)	7.535(1)	arc-melted under Ar, annealed @ 800 °C for 10 d	[14]
Dy_2SnAu_2	7.822(1)	7.503(1)	arc-melted under Ar, annealed @ 800 °C for 10 d	[14]
Ho_2SnAu_2	7.797(1)	7.455(1)	arc-melted under Ar, annealed @ 800 °C for 10 d	[14]
Er_2SnAu_2	7.782(2)	7.396(3)	arc-melted under Ar, annealed @ 800 °C for 10 d	[14]
Tm_2SnAu_2	7.760(3)	7.380(4)	arc-melted under Ar, annealed @ 800 °C for 10 d	[14]
Lu_2SnAu_2	7.728(6)	7.342(6)	arc-melted under Ar, annealed @ 800 °C for 10 d	[14]
Yb_2PbAu_2	8.037(2)	7.465(2)	induction melted in Ta tube under Ar	[39]

Table 1.3 Compounds with the W_2CoB_2 Structure

Compound	*a* (Å)	*b* (Å)	*c* (Å)	Synthesis Conditions	Reference
Ce_2SnNi_2	4.3936(9)	5.7396(9)	8.59679(13)	arc-melted, annealed @ 800 °C for 2 w	[16]
Nd_2SnNi_2	4.360(1)	5.695(2)	8.498(2)	arc-melted, annealed @ 800 °C 2-3 w	[17]
Gd_2SnNi_2	4.294(1)	5.638(1)	8.390(1)	arc-melted, annealed @ 800 °C 2-3 w	[18]
Tb_2SnNi_2	4.278(1)	5.614(1)	8.332(1)	arc-melted, annealed @ 800 °C 2-3 w	[18]
Dy_2SnNi_2	4.247(1)	5.615(1)	8.273(1)	arc-melted, annealed @ 800 °C 2-3 w	[18]

Table 1.4 Compounds with the Mn_2AlB_2 Structure

Compound	*a* (Å)	*b* (Å)	*c* (Å)	Synthesis Conditions	Reference
Y_2InNi_2	3.900(1)	14.186(2)	3.694(1)	arc-melted, annealed under vacuum @ 870 K	[19]
Sm_2InNi_2	3.961(1)	14.370(4)	3.771(2)	arc-melted, annealed under vacuum @ 870 K	[19]
Gd_2InNi_2	3.930(1)	14.240(3)	3.717(2)	arc-melted, annealed under vacuum @ 870 K	[19]
Tb_2InNi2	3.921(1)	14.217(4)	3.694(1)	arc-melted, annealed under vacuum @ 870 K	[19]
Ho_2InNi_2	3.899(1)	14.139(4)	3.658(2)	arc-melted, annealed under vacuum @ 870 K	[19]
Er_2InNi_2	3.893(1)	14.110(4)	3.659(2)	arc-melted, annealed under vacuum @ 870 K	[19]
Tm_2InNi_2	3.886(2)	14.041(3)	3.613(2)	arc-melted, annealed under vacuum @ 870 K	[19]
Lu_2InNi_2	3.855(1)	14.005(4)	3.670(2)	arc-melted, annealed under vacuum @ 870 K	[19]

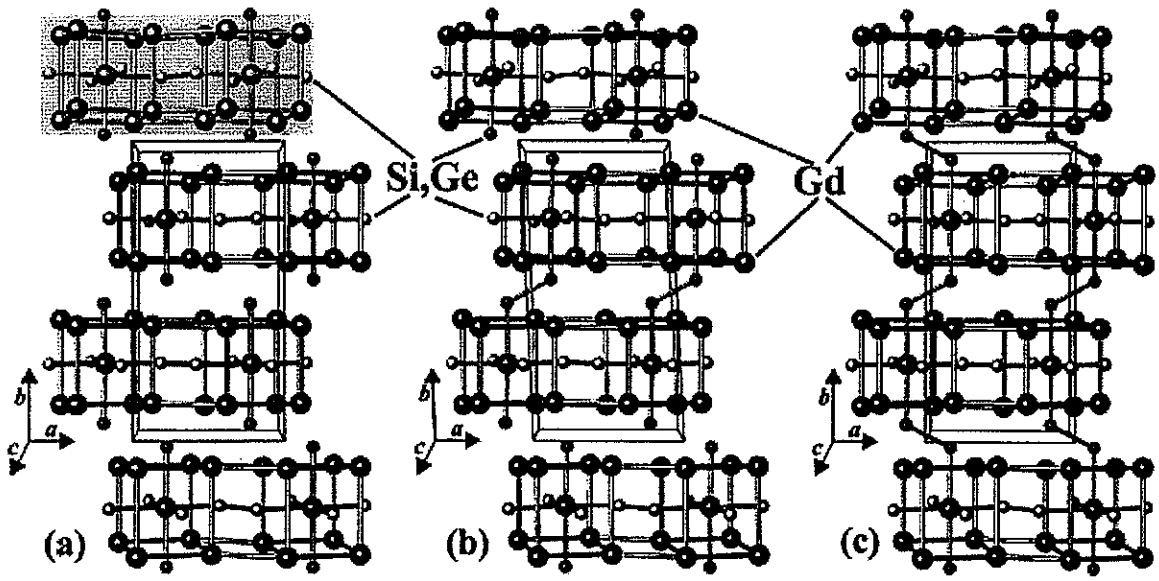

Figure 1.1 $Gd_5(Si_xGe_{1-x})_4$ forms the Sm_5Ge_4-type (a), $Gd_5Si_2Ge_2$-type (b), and Gd_5Si_4-type (c) crystal structures, taken from [20].

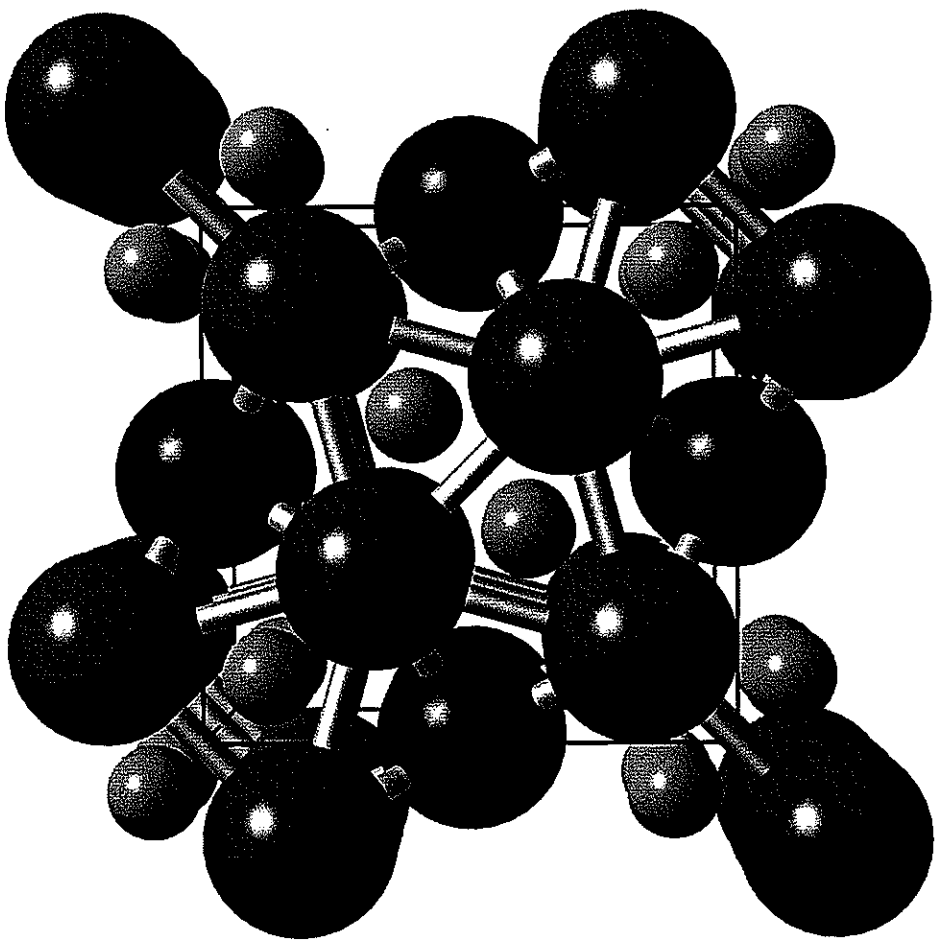

Figure 1.2 A view of the Mo_2FeB_2 structure along the *c* axis, where the gray spheres are Mo atoms, the blue spheres are Fe atoms and the green spheres are B atoms. Bonding between Mo and Fe atoms is shown to highlight the 3^2434 net motif.

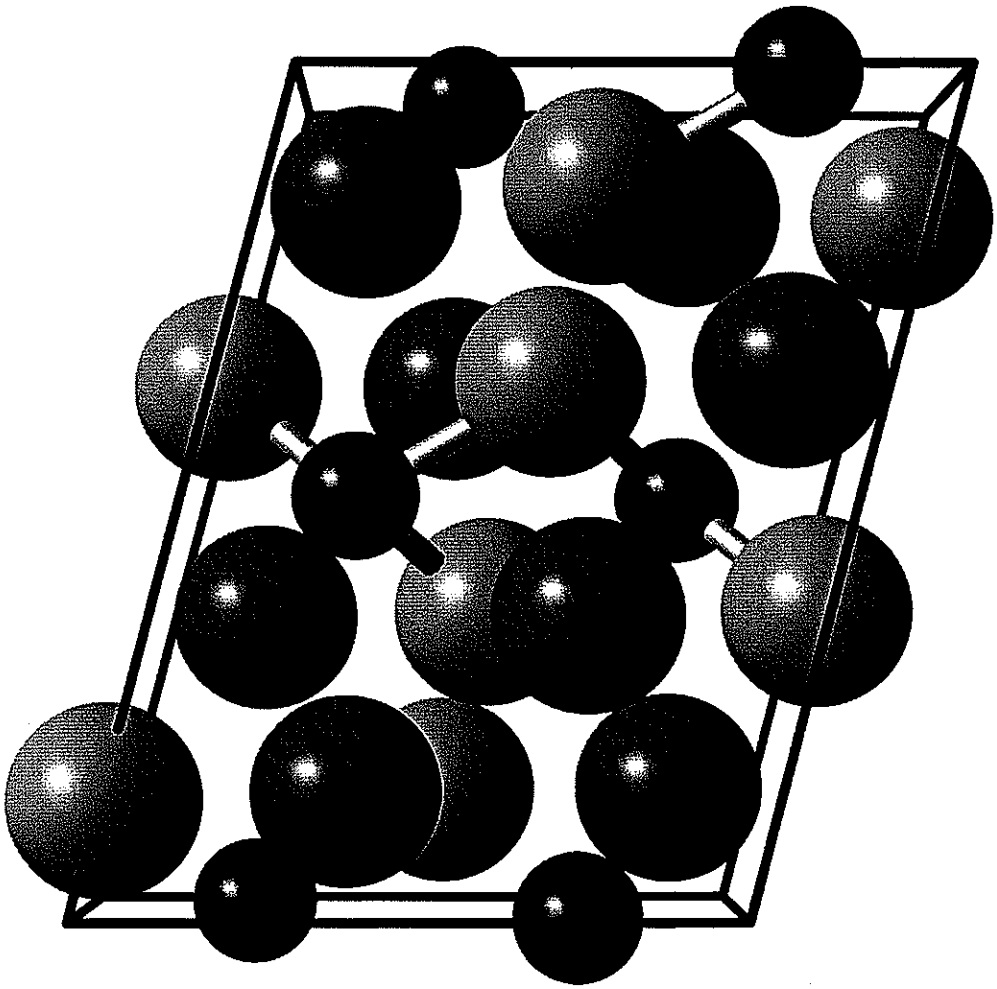

Figure 1.3 A view of the Gd_2AlGe_2 structure down the *b* axis. The gray spheres are Gd atoms and the bonding between Al atoms (blue spheres) and Ge atoms (green spheres) is emphasized.

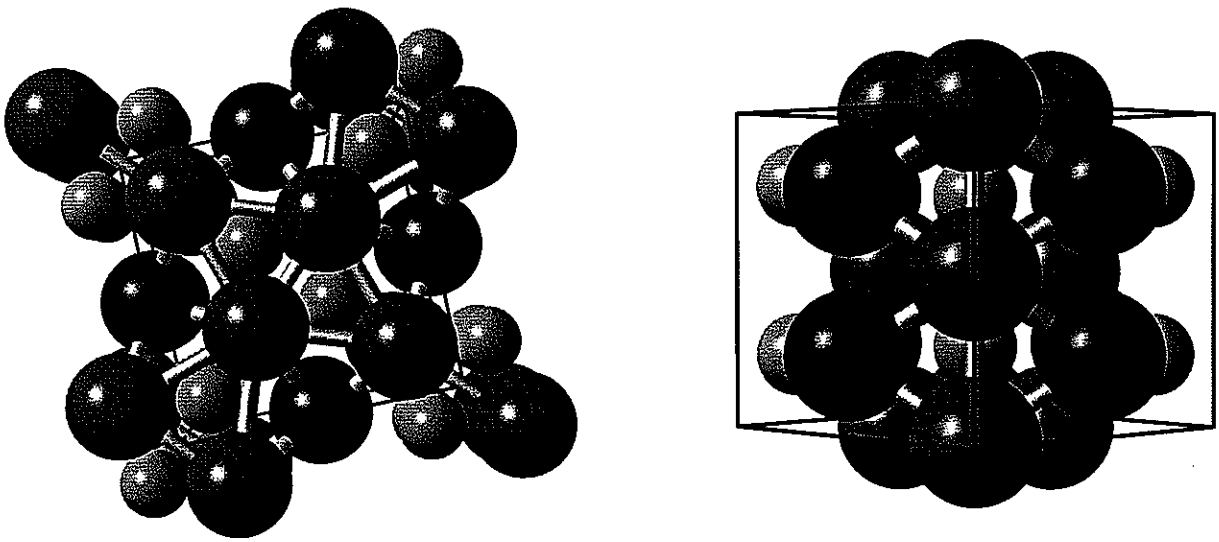

a.) b.)

Figure 1.4 a.) The ternary ordered version of the Zr_3Al_2 structure viewed down the *c* axis, with RE-RE bonding emphasized to show the distorted 3^2434 nets of RE (gray spheres) relative to the X atoms (blue spheres) and M atoms(green spheres). b.) Another view of the ternary version of the Zr_3Al_2 structure, down the [110] direction, where the distortion from the U_3Si_2 structure is more evident.

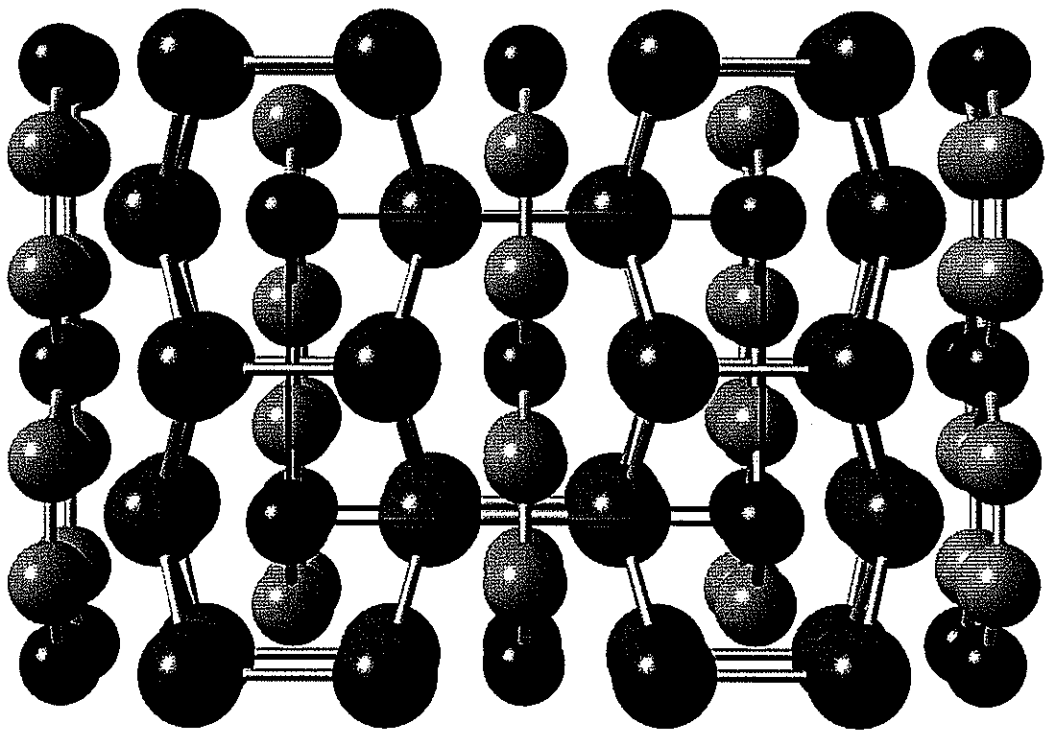

Figure 1.5 A view of the W_2CoB_2 structure down the c axis, where the gray spheres are W atoms, the blue spheres are Co atoms and the green spheres are B atoms.

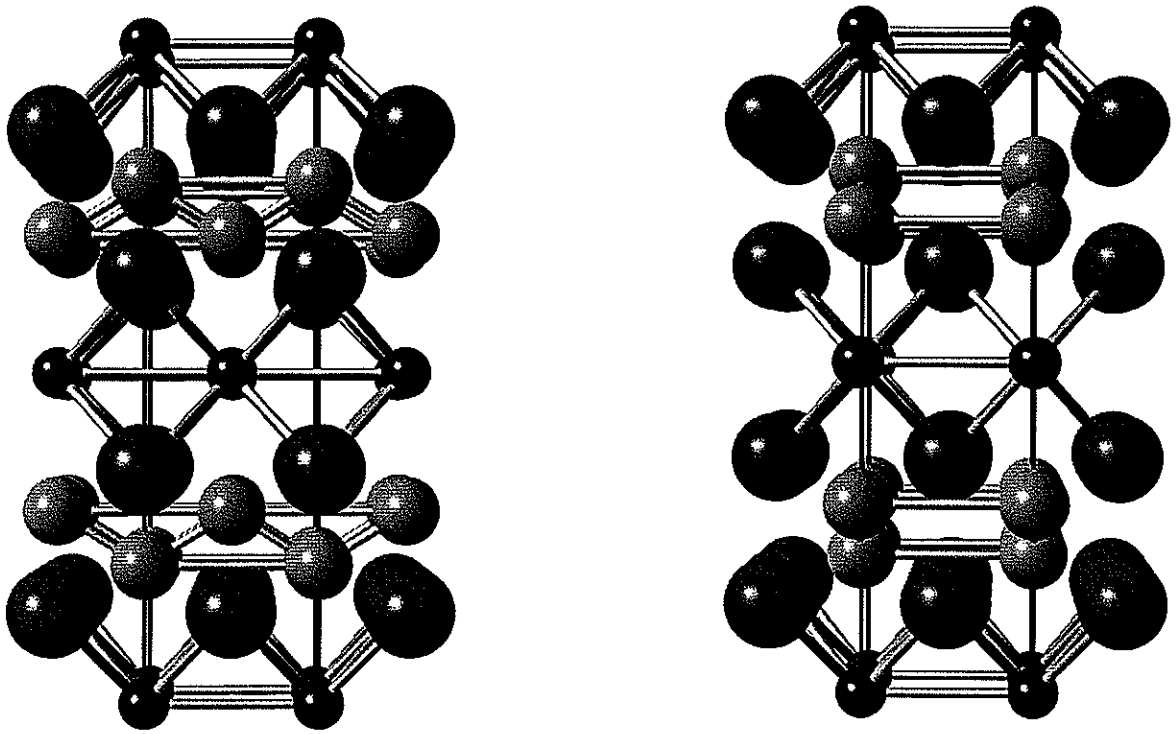

a.) b.)

Figure 1.6 a.) A view of the Mn_2AlB_2 structure down the *a* axis, where the gray spheres are Mn atoms, the blue spheres are Al atoms and the green spheres are B atoms. Bonding is emphasized between B atoms and also between Mn and Al atoms. b.) Another view of the Mn_2AlB_2 structure down the *c* axis.

Gd_2AlGe_2: An "Almost-Zintl Phase" and a New Stacking Variant of the W_2CoB_2 type

A paper published in *Zeitschrift fuer Anorganische und Allgemeine Chemie*, **2002**, 628, 1575.

Wonyoung Choe, Sean McWhorter and Gordon J. Miller

Abstract

The synthesis, structure determination and calculated electronic structure of the new phase, Gd_2AlGe_2, are reported. The title compound crystallizes in a new structure type with space group *C2/c*, a = 10.126(2) Å, b = 5.6837(12) Å, c = 7.7683(16) Å, and β = 104.729(3)°. Tight-binding linear-muffin-tin orbital (TB-LMTO-ASA) calculations show a distinct minimum in the total density of states for this structure at 18 valence electrons per formula unit (Gd_2AlGe_2 has 17 valence electrons in its formula unit), which arises from polar covalent bonding within the three-dimensional [$AlGe_2$] net, Gd-Ge interactions and three-center, two-electron bonding between Al and Gd. The structure is a new stacking variant of the W_2CoB_2 structure type, which is observed for numerous ternary rare-earth silicides and germanides. *Dedicated to Prof. Welf Bronger on the occasion of the 70th anniversary of his birthday.*

Introduction

Classical Zintl phases involve combinations of active metals with more electronegative main group elements from groups 13-16. They are electron precise, valence compounds that show semiconducting behavior. Electronic structure calculations identify

that bonding within the network of the electronegative components is optimized and responsible for the energy gap [1]. Therefore, we can apply the octet rule or other simple electron counting rules to rationalize the observed structure. In the past decade, there have been significant developments toward studying so-called "metallic Zintl phases" or polar intermetallics, in which bonding is optimized within the electronegative metal net, but there is no energy gap [1]. These compounds generally involve combinations of alkali or alkaline earth metals with group 12-14 elements. Perhaps the next stage of development involves the combination of rare earth elements with post-transition elements from groups 13-14. Such compounds may show interesting chemical and physical properties, as, for example, $Gd_5(Si_xGe_{1-x})_4$, which undergo structural phase transitions involving breaking/forming Si/Ge covalent bonds on heating/cooling coupled with a magnetic transition that leads to a giant magnetocaloric effect [2]. This thermal property finds application in magnetic refrigeration [3].

As part of a research effort to identify the coupling of magnetic and crystallographic structures in the $Gd_5(Si_xGe_{1-x})_4$ system, we have attempted to replace some of the Gd atoms by nonmagnetic metal atoms, which have also produced new R_2MT_2 (R = rare earth element; M = nonmagnetic metal; T = Si or Ge) compounds. Previously known compounds in the R_2MT_2 system include two primary structure types: (1) the orthorhombic W_2CoB_2 type for R_2AlSi_2 (R = Er, Ho, Y;) [4], and (2) the tetragonal Mo_2FeB_2 type for Yb_2AlSi_2 [1] and R_2InGe_2 (R = La, Ce, Pr, Nd, Sm, Gd, Tb, Dy, Ho, Yb, Y; Mo_2FeB_2 type) [5, 6]. Recently, we have reported a new addition to the Mo_2FeB_2 family, Gd_2MgGe_2, involving a nonmagnetic Mg atom, which produces a Gd-Ge substructure that resembles part of the structure of Gd_5Ge_4 [7]. In an attempt to increase the valence electron concentration, we

replaced Mg by Al in the Gd_2MGe_2 system, and, surprisingly discovered a new structure type for the R_2MT_2 family, Gd_2AlGe_2. In this paper, we report its synthesis, structure determination and calculated electronic structure to discuss important implications of the chemical bonding in this compound.

Experimental

Synthesis. All elements were used as obtained: Gd (99.999%; Ames Laboratory), Al (99.999%; Johnson Matthey), and Ge powder (99.999+%; 100 mesh, Aldrich). All elements and products were stored and handled in an Ar-filled glove box. Reactions were carried out in sealed Ta ampoules that were enclosed in evacuated, fused silica tubes. Ge (1.28 mmole) powder together with Al (0.64 mmole) and Gd (1.28 mmole) were heated to 1373 K for 7 hr, cooled slowly (ca. 1 K/min) to 938 K, and then quenched in air. In addition to Gd_2AlGe_2, the product contained GdGe according to Guinier X-ray powder diffraction (Cu K_α radiation).

Crystallographic Studies. A crystal of Gd_2AlGe_2 with dimensions 0.068 × 0.069 × 0.070 mm^3 was chosen for the data set collection and mounted at the end of a glass fiber within epoxy. Room temperature (ca. 300 K) X-ray diffraction data of this crystal were collected using a Bruker SMART-1000 CCD diffractometer with Mo K_α radiation (λ = 0.71073 Å) and a detector-to-crystal distance of 5.08 cm. Data were collected in at least a quarter hemisphere and were harvested by collecting three sets of frames with 0.3° scans in ω for an exposure time of 10 sec per frame. The range of 2θ extended from 3.0° to 56.0°. Data were corrected for Lorentz and polarization effects; absorption corrections were based on fitting a function to the empirical transmission surface as sampled by multiple equivalent reflections.

Unit cell parameters were indexed by peaks obtained from 90 frames of reciprocal space images and then refined using all observed diffraction peaks after data integration. The structure solution was obtained by direct methods and refined by full-matrix least-squares refinement of F_o^2 using the SHELXTL 5.12 package [8].

Structure Refinement. The space groups corresponding to the observed systematic extinctions are the monoclinic groups *Cc* and *C2/c*, and we refined the structure in the centrosymmetric group. Initial atomic coordinates obtained from direct methods lead to an isotropic refinement with R = 0.0544 for 12 parameters and 312 reflections. The stoichiometry at this point corresponds to Gd_2AlGe_2. Anisotropic refinement of this model yielded R = 0.0441 and wR = 0.1213. The highest peak in the Fourier difference map is located near Ge at a distance of 1.41 Å with a height of 3.043 e^-/Å. The final refined stoichiometry agrees well with the results of microprobe analysis on the crystal used in X-ray data collection, $Gd_{0.38(4)}Al_{0.24(2)}Ge_{0.38(2)}$ [9]. A summary of the crystallographic data is listed in Table 2.1. Final atomic coordinates and isotropic thermal factors are listed in Table 2.2, anisotropic thermal parameters in Table 2.3, and important bond distances in Table 2.4.

Computational Details. Tight-binding linear muffin-tin orbital (TB-LMTO) electronic band structure calculations were carried out for Gd_2AlGe_2 in the atomic sphere approximation using the LMTO47 program [10]. Exchange and correlation were treated in a local density approximation. All relativistic effects except spin-orbit coupling were taken into account using a scalar relativistic approximation. The radii of the Wigner-Seitz (WS) spheres were obtained by requiring the overlapping potential to be the best possible approximation to the full potential according to an automatic procedure – no empty spheres were necessary [11]. The WS radii determined by this procedure for the atoms in Gd_2AlGe_2 are 1.976 Å for Gd,

1.547 Å for Al and 1.496 Å for Ge. The basis set included Gd 6*s*, 6*p* and 5*d* orbitals, Al 3*s*, 3*p* and 3*d* orbitals and Ge 4*s*, 4*p* and 4*d* orbitals. The Gd 4*f* orbitals were treated as core functions with seven valence electrons. Furthermore, the Al 3*d* and Ge 4*d* orbitals were treated by the Löwdin downfolding technique [10]. The **k**-space integrations to determine the self-consistent charge density, density of states and crystal Hamiltonian orbital populations (COHP) were performed by the tetrahedron method using 68 **k**-points in the irreducible wedge of the *C*-centered monoclinic cell.

Results and Discussion

The monoclinic structure of Gd_2AlGe_2 is illustrated in Figure 2.1 and emphasizes the three-dimensional [$AlGe_2$] network in which the Al is four-bonded to Ge atoms in a slightly distorted "sawhorse" geometry while the Ge atoms are planar three-bonded to two Al atoms and one other Ge atom. The Ge–Ge distance of 2.64 Å is noticeably longer than in other compounds such as Gd_2MgGe_2 (2.56 Å) [7] and R_2InGe_2 (2.42-2.54 Å; R = La-Sm, Gd-Ho, Yb, Y) [5, 6]. Moreover, the Al-Ge distances (2.68 Å) are also longer than those in other R-Al-Ge systems, e.g., 2.58-2.62 Å in $Ca_3Al_2Ge_3$ [12].

The Gd atoms occupy voids in the [$AlGe_2$] net – the three dimensional arrangement resembles a distorted cubic close packing, but a careful analysis of the Gd–Gd distances identifies a series of puckered 6^3 Gd nets (see Figure 2.2a) that are centered by Al atoms. From this perspective, the structure of Gd_2AlGe_2 can be related to the W_2CoB_2 family of structures, as seen for Y_2AlSi_2 [4] (see Figure 2.2b). In this orthorhombic structure, the [$AlSi_2$] net is planar with four-bonded Al and three-bonded Si atoms in Si–Si dimers, but the Y atoms form the same puckered 6^3 net with Al atoms in the centers of the puckered

hexagons. The striking difference between the two structure types is how the Si–Si or Ge–Ge dimers are connected to Al atoms. In ternary A-Al-T or R-Al-T systems (A = alkali earth; R = rare earth; T = Si or Ge) Al atoms are tetrahedrally coordinated by the T element, as exemplified by $Ca_3Al_2Ge_3$ [12], Y_2AlGe_3 [13], $GdAl_2Si_2$ [14], $Ce_3Al_4Si_6$ [15], $CeAlSi_2$ [15] and $Yb_7Al_5Ge_8$ [16]. Interestingly, in both Gd_2AlGe_2 and Y_2AlSi_2, the Al atoms are four coordinate, but in different ways. As we have mentioned, the coordination environment around Al atoms in Gd_2AlGe_2 is four-connected, "sawhorse" type (trigonal bipyramidal minus one equatorial ligant), while in Y_2AlSi_2 it is four-connected (rectangular) planar. The Al geometry of the latter type can be seen in other ternary R-Al-T systems such as $La_2Al_3Ge_4$ [17] and Yb_2AlSi_2 [4]. However, the Al geometry in the new compound Gd_2AlGe_2 is unprecedented, to the best of our knowledge. Such four-connected "sawhorse" coordination is frequently found around Sb atoms, for example, in various antimony sulfide anionic networks such as $Sb_4S_7^{2-}$ [18] and $Sb_8S_{13}^{2-}$ [19].

Therefore, how can we count electrons in Gd_2AlGe_2 to account for its observed structure? According to the Zintl-Klemm-Busmann counting rules [1], we use the connectivity of the $[AlGe_2]$ net to establish its charge: Al is four-bonded (isoelectronic with Si) and Ge is three-bonded (isoelectronic with As), so the formal charge on the $[AlGe_2]$ net would be 3–, i.e., 14 valence electrons. In Gd_2AlGe_2 there are 3 additional valence electrons that may be accommodated in metal-metal bonding states, which must be ascertained by electronic structure calculations. From another viewpoint, we can also use the local coordination at Al and Ge atoms: each Al is surrounded by a "sawhorse" geometry; each Ge by a trigonal planar geometry. The Al sites would be assigned 6 valence electrons (4 bonding electrons + 1 nonbonding electron pair); the Ge sites would be assigned 4 valence

electrons (3 σ-bonding electrons + 1 π-bonding electron). This also gives 14 valence electrons for the [$AlGe_2$] network. In the following section, we examine how these simple electron counting guides compare with the results of electronic structure calculations.

Calculated Electronic Structure: The total density of states (DOS) and projection of the [$AlGe_2$] states calculated by the TB-LMTO-ASA method are illustrated in Figure 2.3. Also, the COHP curves for the shortest Ge–Ge, Al–Ge and Gd–Ge contacts are shown. Table 2.5 summarizes important details from these calculations. The Fermi level for Gd_2AlGe_2 falls just below a deep minimum in the DOS curve, which corresponds to the region where bonding Gd–Ge interactions would be optimized (see COHP curve), at 18 valence electrons per formula unit. The COHP curves indicate that Ge–Ge and Al–Ge antibonding states are already occupied in Gd_2AlGe_2, while Gd–Ge bonding states are not yet filled. Therefore, with 17 valence electrons per formula unit, Gd_2AlGe_2 adopts a structure that optimizes the combination of "cation-anion" interactions.

Magnification of the DOS near the Fermi level for "nonmagnetic" Gd_2AlGe_2 shows that the Fermi level does lie at a relative minimum of the DOS, which suggests little driving force for magnetic ordering. We carried out spin polarized calculations on four different models of magnetic ordering: one completely ferromagnetic ordering of magnetic moments at the Gd sites (FM) and three different antiferromagnetic ordering models (AFM-1, AFM-2, AFM-3; see Figure 2.4). All magnetic ordering models have a lower calculated total energy than the nonmagnetic case, which is due largely to the exchange splitting of the 4*f* states. Furthermore, although the ferromagnetic model is the lowest energy model, the antiferromagnetic model AFM-3 is just 8 meV/formula unit above it. Thus, we conclude that Gd_2AlGe_2 remains paramagnetic down to low temperatures. Furthermore, all magnetically

ordered models give higher DOS values at the Fermi level than the nonmagnetic case, which is another indication of stability of the nonmagnetic model. Accurate measurement demands a single phase product, and we are still working to achieve these measurements.

What accounts for the minimum in the DOS at 18 valence electrons? Analysis of the electronic band structure and the DOS finds 7 occupied states associated with the Ge–Ge dimer, which leads to cylindrically symmetrical electron density about the Ge–Ge dimer (see Figure 2.5). There are also 2 additional states, which involve a mixture of an Al 3*s*-3*p* hybridized orbital and Gd 6*s* and 5*d* orbitals. The monoclinic symmetry of Gd_2AlGe_2 makes an orbital analysis cumbersome, but an examination of the electron density near Al shows two regions of three-center two-electron bonding with a pair of Gd atoms separated by 3.55 Å (see Figure 2.5). In this way, we can account for the minimum in the DOS curve at 18 valence electrons or 9 orbitals per formula unit.

As a final point, we indicated that the Ge–Ge distance in this compound is long compared to other examples, which include structures adopting the tetragonal Mo_2FeB_2-type and the orthorhombic W_2CoB_2-type. In a future article, we will report on factors influencing the adoption of these different structure types among R_2MT_2 compounds (R = rare-earth element; M = various metal atoms; T = Si or Ge), but preliminary electronic structure calculations suggest a significant size influence to form the monoclinic Gd_2AlGe_2-type structure rather than the tetragonal or orthorhombic structures found for Gd_2MgGe_2 or Y_2AlSi_2. Regarding the long Ge–Ge distance, the site symmetry for this dimer is C_i in Gd_2AlGe_2, whereas the site symmetries for similar dimers in the other structure types are both D_{2h}. For an isolated, homonuclear diatomic molecule (or molecular ion), 7 occupied orbitals correspond to σ_s, σ_s^*, σ_p, π and π^*, while the unoccupied orbital is σ_p^*. From the

DOS and band structure, the σ_s and σ_s* states for the Ge–Ge dimer lie ca. 8 eV below the Fermi level in Gd_2AlGe_2. Thus, for the following discussion, we focus just on the *p* orbitals. For the dimer in site symmetry C_i, the orbitals transform as follows: σ_p as a_g; π as $2a_u$; π* as $2a_g$; and σ_p* as a_u. Therefore, symmetry allows mixing between π-bonding and σ_p-antibonding orbitals. In site symmetry D_{2h}, the orbitals transform as follows: σ_p as a_g; π as $b_{1u} + b_{3u}$; π* as $b_{2g} + b_{3g}$; and σ_p* as b_{2u}, which means that the σ_p-antibonding orbital is not allowed to mix with any of the other orbitals. We can conclude from this symmetry argument that the long Ge–Ge distance in Gd_2AlGe_2 arises from the symmetry-allowed mixing of σ_p* into the bonding orbitals of the Ge–Ge dimer, which remains forbidden in the tetragonal and orthorhombic structure alternatives.

Summary

In this article, we reported a new compound, Gd_2AlGe_2, which adopts a new monoclinic structure type. Electronic structure calculations were useful to account for various structural features as well as to predict a slight preference for ferromagnetic behavior at low temperatures. We continue to investigate such new ternary rare-earth tetrelides as part of a larger program to study magnetic refrigeration materials.

Acknowledgements

This work was supported by the Materials Science Division, Office of Basic Energy Sciences, U. S. Department of Energy.

References

[1] G. J. Miller in *Chemistry, Structure and Bonding of Zintl Phases and Ions*, Ed. S. M. Kauzlarich, VCH Publishers, Inc., New York, 1996, p. 1 and references therein.

[2] (a) V. K. Pecharsky, K. A. Gschneidner, Jr., *Phys. Rev. Lett.* **1997**, *78*, 4494;

(b) V. K. Pecharsky, K. A. Gschneidner, Jr., *Appl. Phys. Lett.* **1997**, *70*, 3299;

(c) V. K. Pecharsky, K. A. Gschneidner, Jr., *J. Magn. Magn. Mater.* **1997**, *167*, L179;

(d) A. Giguere, M. Foldeaki, R. Ravi Gopal, T. K. Bose, A. Frydman, *Phys. Rev. Lett.* **1999**, *83*, 2262;

(e) K. A. Gschneidner, Jr., V. K. Pecharsky, E. Brück, H. G. M. Duijin, E. M. A. Levin, *Phys. Rev. Lett.* **2000**, *85*, 4190.

[3] V. K. Pecharsky, K. A. Gschneidner, Jr., *J. Magn. Magn. Mater.* **1999**, *200*, 44.

[4] C. Kranenberg, and A. Mewis, *Z. anorg. allg. Chem.* **2000**, *626*, 1448.

[5] V. I. Zaremba, A. Stepien'-Damm, G. P. Nichiporuk, Y. B. Tyvanchuk, Y. M. Kalychak, *Kristallografiya* **1998**, *43*, 13.

[6] V. I. Zaremba, Y. B. Tyvanchuk, J. Stepien-Damm, *Z. Kristallogr. New Cryst. Struct.* **1997**, *212*, 291.

[7] W. Choe, G. J. Miller, E. M. Levin, *J. Alloys Comp.* **2001**, *329*, 121.

[8] SHELXTL, Bruker Analytical X-ray Instruments, Inc., Madison, WI, 2001.

[9] Further details of crystal structure are available from Fachunfomationszentrum Karlruhe, D-76344 Eggenstein-Leopoldshafen, Germany (email: shoe@fiz-karlsruhe.de) under CSD-XXXX.

[10] (a) O.K. Andersen, *Phys. Rev. B* **1975**, *B12*, 3060;

(b) O.K. Andersen, O. Jepsen, *Phys. Rev. Lett.* **1984**, *53*, 2571;

(c) O.K. Andersen, O. Jepsen, D. Glötzel, in *Highlights of Condensed-Matter Theory*, Eds. F. Bassani, F. Fumi, M.P. Tosi: North-Holland, New York, 1985;

(d) O.K. Andersen, *Phys. Rev. B* **1986**, *B34*, 2439.

[11] O. Jepsen, O.K. Andersen, *Z. Phys. B* **1995**, *97*, 35.

[12] G. Cordier, H. Schäfer, *Z. anorg. allg. Chem.* **1982**, *490*, 136.

[13] D. Johrendt, A. Mewis, *Z. anorg. allg. Chem.* **1996**, *622*, 589.

[14] R. Nesper, H. G. Von Schnering, J. Curda, *Z. Naturforsch. B* **1982**, *37B*, 1514.

[15] H. Flandorfer, P. Rogl, *J. Solid State Chem.* **1996**, *127*, 308.

[16] J. T. Zhao, E. Parthé, *Acta Crystallogr., Sect. C Cryst. Struct. Commun.* **1991**, *C47*, 1.

[17] J. T. Zhao, E. Parthé, Zhao, *Acta Crystallogr., Sect. C: Cryst. Struct. Commun.* (1991), C47(9), 1781-4.

[18] D. V. Pushkin, V. N. Serezhkin, Y. A. Buslaev, Y. N. Mikhailov, *Zh. Neorg. Khim.* (1999), 44(5), 781-789.

[19] K. Volk, H. Schaefer, *Z. Naturforsch., B: Anorg. Chem., Org. Chem.* (1979), 34B (12), 1637-40.

Table 2.1. Crystallographic data for Gd_2AlGe_2

Empirical formula	Gd_2AlGe_2
Crystal system	Monoclinic
Space group	*C2/c* (No. 15)
Z	4
a (Å)	10.126(2)
b (Å)	5.6837(12)
c (Å)	7.7683(16)
β (°):	104.729(3)
V (Å^3)	432.38(16)
Density (calc., g·cm^{-3})	7.476
No. refl. Collected	899
No. unique refl.	312
No. obs. refl. ($I \geq 2\sigma(I)$)	278
No. parameters refined	25
R / wR2 (obs. data)	0.0402 / 0.1192
R / wR2 (all data)	0.0441 / 0.1213
Goodness of Fit (obs. / all)	1.153 / 1.153
Mean shift	0.000
Max. shift	0.000
Residual electron density:	3.043 and –2.447 e$^-$/Å^3

Table 2.2. Atomic coordinates and isotropic thermal displacement parameters for Gd_2AlGe_2.

Atom	x	y	z	U_{eq}
Gd	0.35526(8)	0.12987(15)	0.85259(11)	0.0060(7)
Al	0	0.1636(14)	¾	0.0063(18)
Ge	0.1385(2)	0.1295(3)	0.4984(3)	0.0099(8)

Table 2.3. Anisotropic thermal parameters for Gd_2AlGe_2.

Atom	U_{11}	U_{22}	U_{33}	U_{23}	U_{13}	U_{12}
Gd	0.0112(9)	0.0039(9)	0.0033(9)	0.0003(3)	0.0028(5)	0.0000(4)
Ge	0.0164(13)	0.0085(13)	0.0057(13)	0.0004(8)	0.0044(10)	0.0002(8)
Al	0.011(4)	0.004(4)	0.005(4)	0	0.004(3)	0

Table 2.4. Important interatomic distances (Å) for Gd_2AlGe_2.

Atom–Atom	Distance (Å)	Atom–Atom	Distance (Å)
Ge–Ge	2.636(4)	Al–Ge	2.663(5); 2×
			2.686(2); 2×
Gd–Ge	3.052(2)		
	3.061(2)	Gd–Gd	3.550(2)
	3.065(2)		3.665(1); 2×
	3.066(2)		
	3.089(2)	Al–Gd	3.225(7)
	3.119(2)		3.280(3)

Table 2.5. Results from TB-LMTO-ASA calculations on nonmagnetic (NM) and various magnetic models (FM, AFM-1, AFM-2, AFM-3) of Gd_2AlGe_2.

	NM	FM	AFM-1	AFM-2	AFM-3
Energy (eV)[a]	17.35	0	0.0498	0.0389	0.0081
E_F (eV)	−1.683	−1.632			−1.632
$N(E_F)$	56.31	71.81			101.72
Orbital Occup.					
Gd 6*s*	0.56	0.29 / 0.28[b]			0.29 / 0.27[b]
Gd 6*p*	0.78	0.40 / 0.38[b]			0.40 / 0.38[b]
Gd 5*d*	2.08	1.17 / 0.91[b]			1.14 / 0.93[b]
Al 3*s*	1.06	0.52 / 0.54[b]			0.53 / 0.52[b]
Al 3*p*	1.43	0.71 / 0.73[b]			0.72 / 0.72[b]
Al 3*d*	0.27	0.14 / 0.13[b]			0.13 / 0.14[b]
Ge 4*s*	1.40	0.69 / 0.71[b]			0.70 / 0.70[b]
Ge 4*p*	2.14	1.06 / 1.08[b]			1.07 / 1.07[b]
Ge 4*d*	0.16	0.08 / 0.07[b]			0.08 / 0.08[b]
Local Moments					
Gd	---	7.30			7.25
Al	---	−0.02			0.01
Ge	---	−0.02			0.01
COHP (eV)					
Ge–Ge	−0.122				
Al–Ge	−0.135;				
	−0.121				
Gd–Ge	−0.071				
	−0.082				
Gd–Gd	−0.029				
	−0.037				

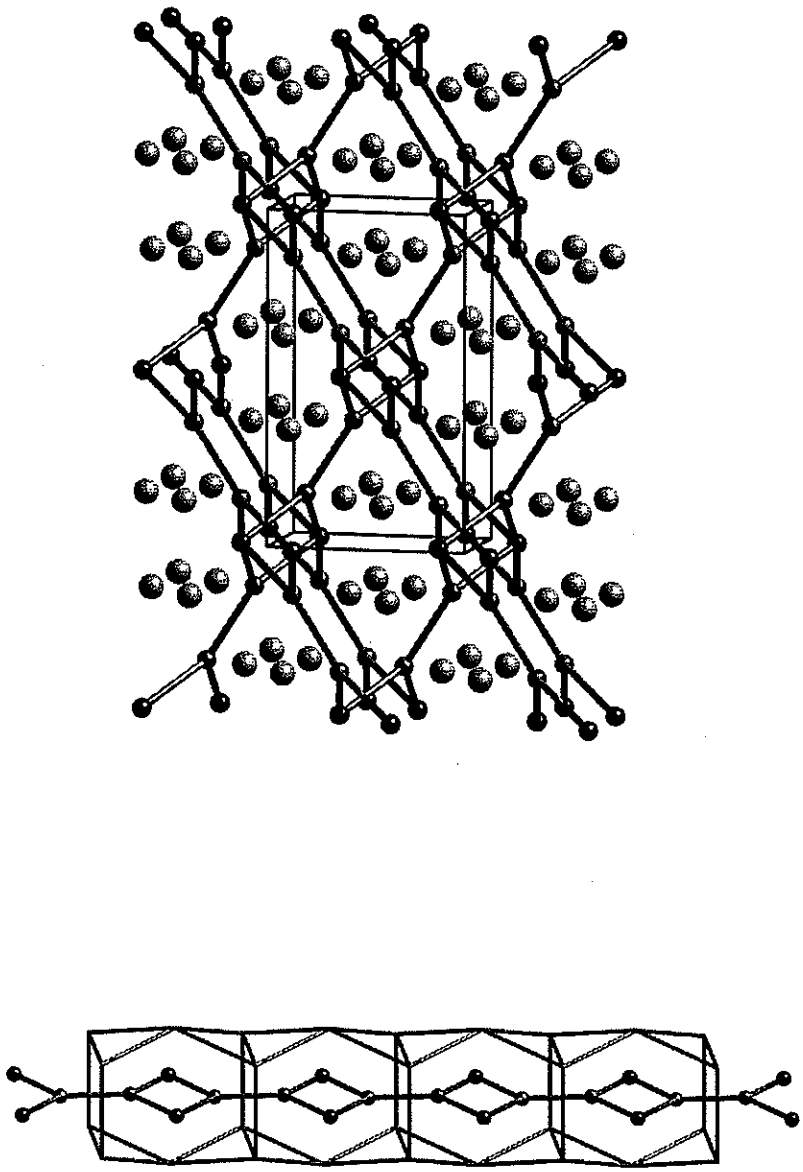

Figure 2.1. Perspective of the structure of Gd_2AlGe_2 with respect to the [001] direction.

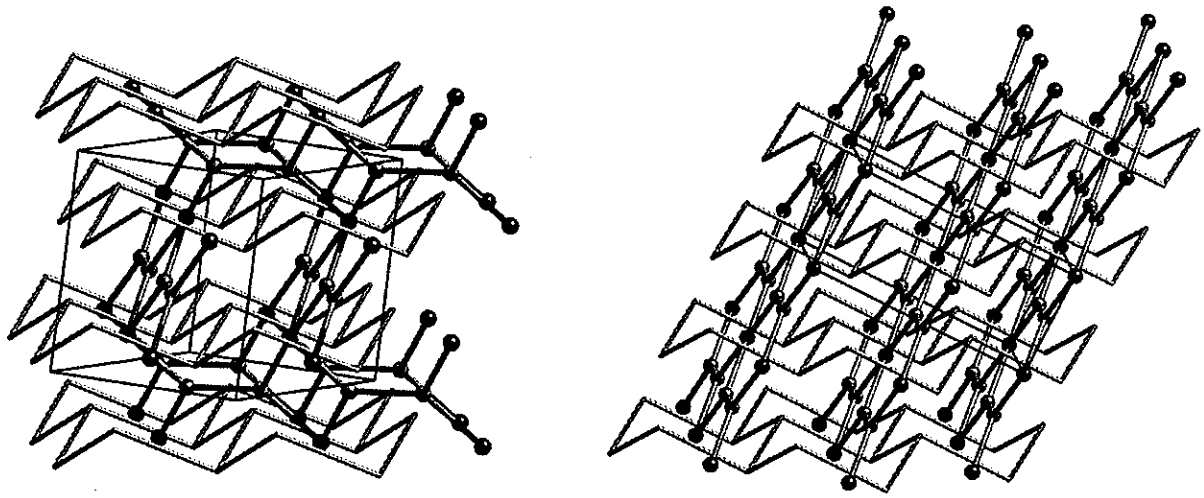

Gd_2AlGe_2 **Y_2AlSi_2**

Figure 2.2. (a) Structure of Gd_2AlGe_2 emphasizing the short Gd–Gd contacts and the sheets of puckered 6^3 nets of Gd atoms; (b) the orthorhombic W_2CoB_2-structure of Y_2AlSi_2 emphasizing the short Y–Y contacts and the sheets of puckered 6^3 nets of Y atoms to display the relationship between the two structure types.

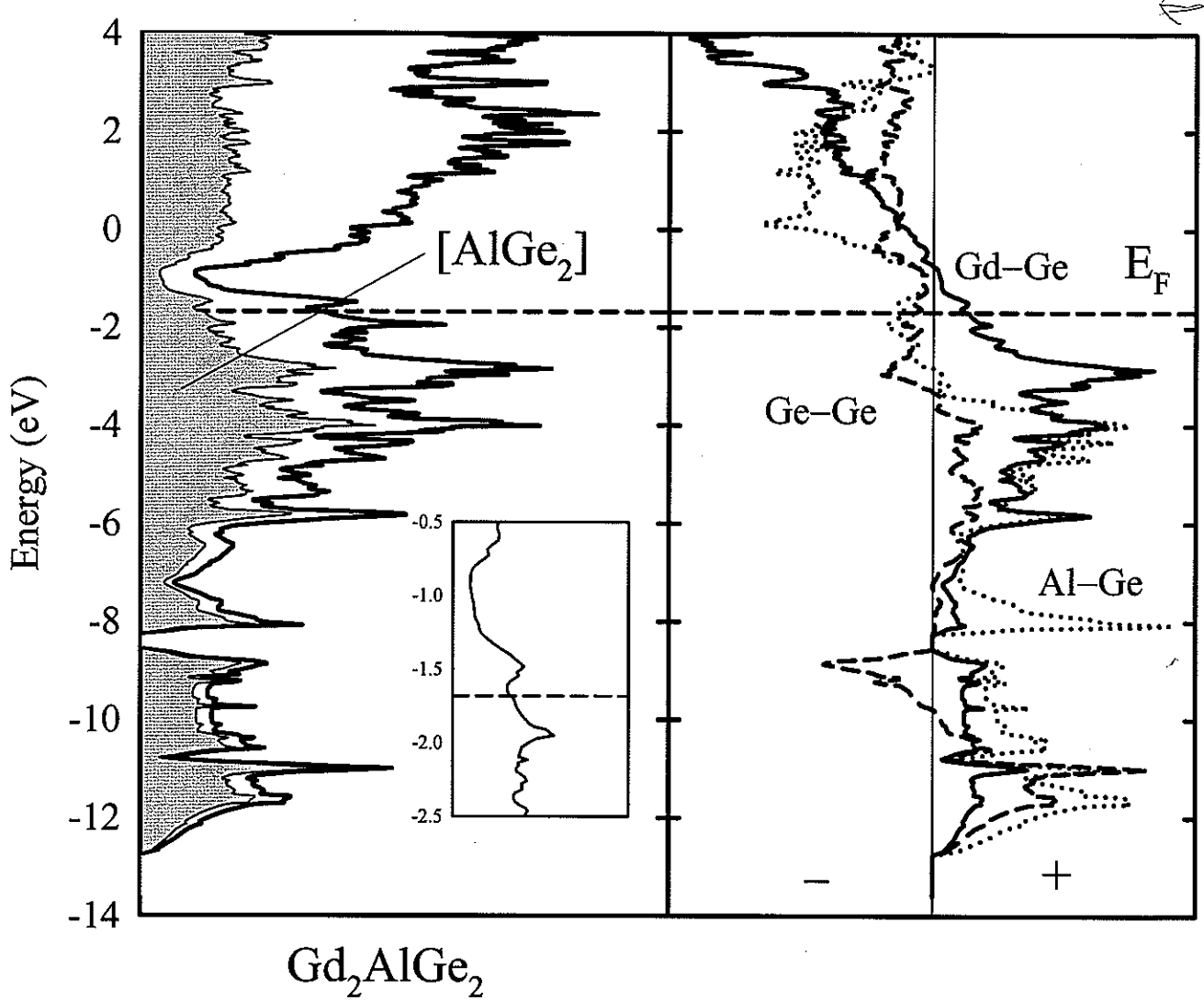

Figure 2.3. (Left) Total DOS and partial DOS (shaded) from the [$AlGe_2$] network for nonmagnetic Gd_2AlGe_2. The insert shows a magnified section near the Fermi level. (Right) COHP curves for Ge–Ge, Al–Ge and Gd–Ge interactions in nonmagnetic Gd_2AlGe_2. The dashed line indicates the Fermi level.

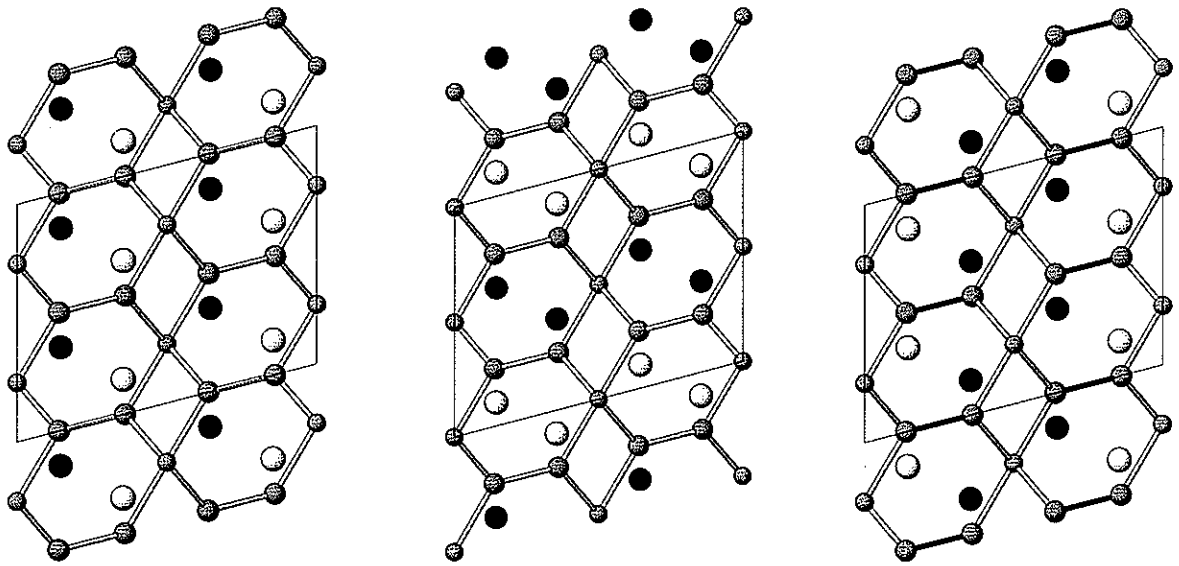

AFM-1 **AFM-2** **AFM-3**

Figure 2.4. Three different antiferromagnetic models of Gd_2AlGe_2 used for spin polarized calculations.

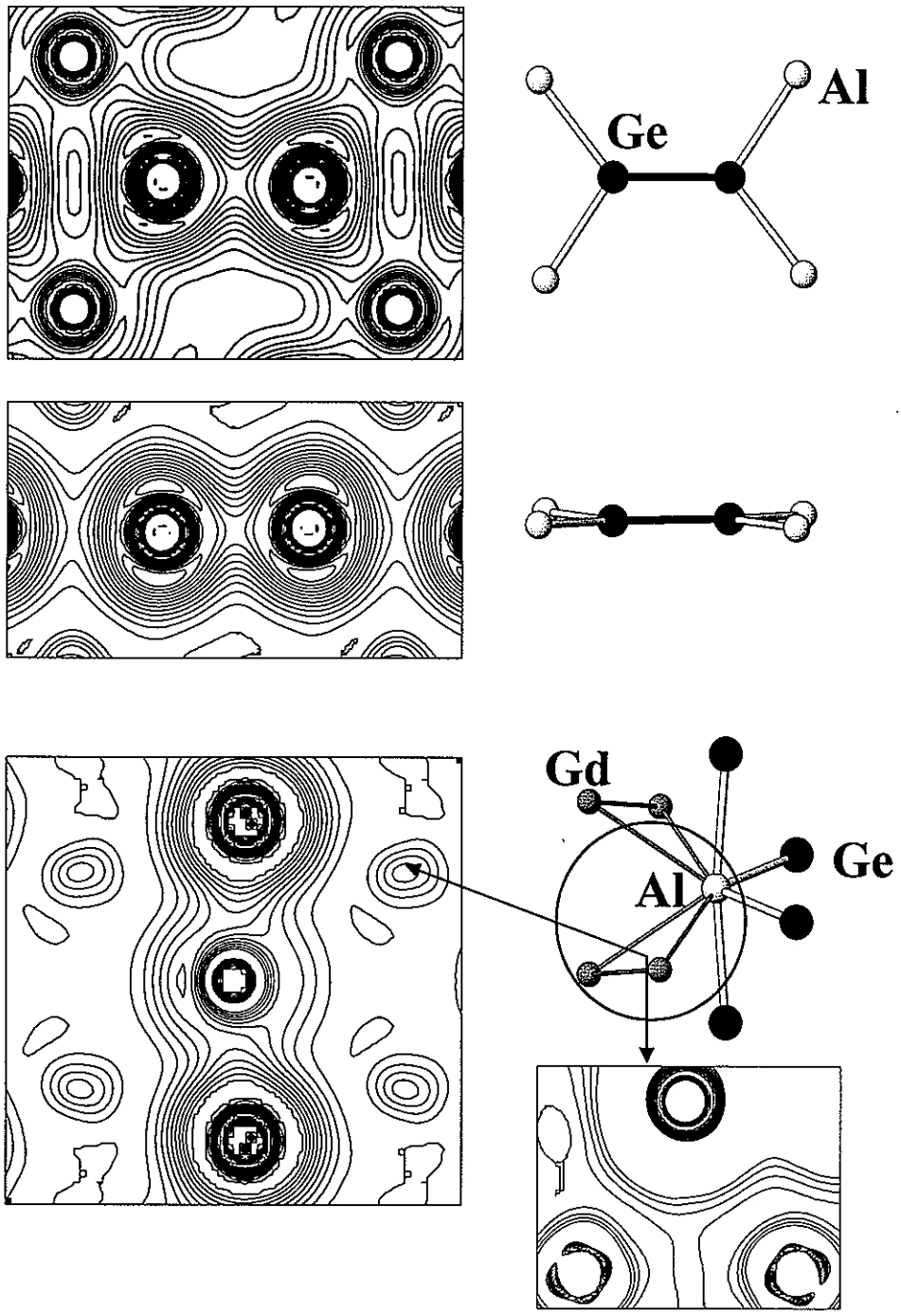

Figure 2.5. Projections of the total valence electron density for various important structural fragments of Gd_2AlGe_2.

Analysis of U_3Si_2 and Zr_3Al_2 Crystal Structures

Introduction

In the first chapter of this thesis, a review of compounds with the composition R_2XM_2 (R=rare earth, X=main group element, M=transition metal, Si, Ge) was made, and these compounds were found to crystallize in one of five crystal structure types: the Mo_2FeB_2-type, the Zr_3Al_2-type, the W_2CoB_2-type, the Mn_2AlB_2 and the Gd_2AlGe_2-type. Upon looking at a system where X and M are fixed and R is varied, it can be seen that in some cases a structural change occurs. An example of this can be seen in the system R_2SnAu_2 (R=lanthanides), where the Gd and Tb compounds adopt the Mo_2FeB_2 (ternary U_3Si_2) structure and the Dy-Lu compounds adopt the Zr_3Al_2 structure [1, 2]. Also, in the system R_2InAu_2, there is a transition from the U_3Si_2 structure type to the Zr_3Al_2 structure type that occurs as R is varied from Er to Tm. Here, the La-Er compounds form the U_3Si_2 structure, while the Tm and Lu analogues adopt the Zr_3Al_2 structure [3]. Finally, one compound, U_2InPt_2, has been observed to crystallize in either the U_3Si_2 or Zr_3Al_2 structure type, depending on the synthetic conditions. Arc-melting the starting materials under Ar has been shown to yield polycrystalline U_2InPt_2 with the U_3Si_2 structure, while preparing U_2InPt_2 using a modified mineralization technique yields single crystalline U_2InPt_2 with the Zr_3Al_2 structure [4, 5].

Electronic structure calculations have been done for Zr_2SnNi_2 and Zr_2InNi_2, showing that the Zr_3Al_2 structure is very slightly favored over the U_3Si_2 structure by only a few kJ/mol. Pöttgen and Dronskowski offer a geometrical explanation for the formation of the Zr_3Al_2 structure, i.e. that those compounds with the smallest rare earth elements adopt the Zr_3Al_2 structure. This is used to propose that the Zr atom in Zr_2InNi_2 and Zr_2SnNi_2 is smaller than the Sc atom in Sc_2InNi_2, leading to the formation of the Zr_3Al_2 structure [6].

In order to help better understand the reasons for the preference of the Zr_3Al_2 structure over the U_3Si_2 structure, or the Zr_3Al_2 aristotype, a series of calculations were performed using the tight-binding LMTO method. As discussed previously, the Zr_3Al_2 structure is a distorted superstructure of the U_3Si_2 structure. Both structures feature 3^2434 nets of Zr or U atoms, with U and Si or Zr and Al sitting in the cubic and trigonal prismatic voids between the 3^2434 nets, respectively. In U_3Si_2, these nets are perfectly aligned along the *c* axis, but in Zr_3Al_2, a distortion occurs and neighboring layers are no longer eclipsed, forming an A-B stacking along the *c* axis, with an angle of 165.9° between them created by the 4_2 axis.

In order to make comparisons between these two structure types using TB-LMTO, a series of eight models were created. The first model was based on the composition Zr_3Al_2, but with the U_3Si_2 structure, which has space group *P4/mbm* and *Z*=2. In the unit cell for this structure there are 12 Zr atoms and 8 Al atoms, with lattice parameters a= 7.630 Å and c= 6.998 Å. Another model was based on the real crystal structure of Zr_3Al_2, with space group $P4_2/mnm$ and *Z*=4. The *c* axis of Zr_3Al_2 with the U_3Si_2 structure was doubled in order to yield the same number of atoms in the same volume as the second model. The other six models are based on intermediate structures, combining the features of both the Zr_3Al_2 and U_3Si_2 structures, as described below. Atomic coordinates for each model are given in Table 3.1.

As previously noted, it is possible to rearrange the atoms in a unit cell with space group *P4/mbm* to form a unit cell with space group symmetry $P4_2/mnm$, and vice versa. In the analysis of this problem, two benchmark models were first constructed: a model with composition Zr_3Al_2 and space group *P4/mbm* (designated Model 1) and a model with composition Zr_3Al_2 and space group $P4_2/mnm$ (designated Model 4, which is the observed

structure of Zr_3Al_2). There are three key elements in the transformation of Model 1 to Model 4, which can be seen as the distortion of an idealized regular structure to the distorted real structure. The first element is the position of the Zr atoms in the *ab* plane. As the Zr atoms move from being eclipsed along the *c* axis, the regular 3^2434 nets become distorted. The irreducible representation associated with this movement is b_{1u}. The second key transformation element is the position of the Al atoms in the *ab* plane. Similar to the net of Zr atoms, the 3^2434 net of Al atoms also becomes distorted. This vibrational mode of the Al atoms also has the irreducible representation of b_{1u}. The third transformation element is the position of the Al atoms relative to a plane. In the undistorted structure (Model 1), the Al atoms are all planar, but upon transformation to the distorted structure, the Al atoms no longer all lie in the same plane. The symmetry of this vibrational mode is b_{1u}.

There are several ways of combining these vibrational modes in order to convert the idealized Model 1 into the distorted Model 4. These have been broken down into two schemes, I and II, in order to make the process easier to visualize. Scheme I concentrates on the effects that moving the Al atoms has on the structure, while Scheme II focuses on the effects of the movement of the Zr atoms (see Figures 3.1 and 3.2).

In Scheme I, the first model used is Model 1, with space group *P4/mbm*. The movement of the Al atoms can be decoupled into their components in the *ab* plane and along the *c* axis. Two models were created based on the vibrations of Al: Model 2A, based on the movement of Al along *c*, and Model 2B, based on the movement of Al in the *ab* plane. Continuing with the focus of Scheme I on the Al atoms, the Al atoms are adjusted to the distorted positions in the unit cell (i.e. the positions of Al in the Zr_3Al_2 structure), creating

Model 3, which can be reached from either Model 2A or 2B. Finally, the Zr atoms are moved to their distorted positions, creating Model 4.

Alternatively, the effects of the movement of the Zr atoms can be focused on, as in Scheme II. The initial positions of the atoms are again given by Model 1, but now the first change to the unit cell is made in moving the Zr atoms to their distorted positions (i.e. the position of the Zr atoms in the Zr_3Al_2 structure), creating Model 5. From Model 5, it is again possible to choose to either displace the Al atoms along the *c* axis, or to their distorted positions in the *ab* plane. Consequently, Model 6A (Al with displaced *c* position) and Model 6B (Al with displaced *ab* positions) are created. From either Model 6A or 6B, the Al is displaced in the remaining direction, once again yielding Model 4.

Experimental

Tight-binding linear muffin-tin orbital (TB-LMTO) electronic band structure calculations were carried out for Zr_3Al_2 in various structures related to the U_3Si_2 and Zr_3Al_2 structure types in the atomic sphere approximation using the LMTO47 program. Exchange and correlation were treated in a local density approximation. All relativistic effects except spin-orbit coupling were taken into account using a scalar relativistic approximation. The radii of the Wigner-Seitz (WS) spheres were obtained by requiring the overlapping potential to be the best possible approximation to the full potential according to an automatic procedure – some empty spheres were necessary in Models 2A, 5 and 6B. The WS radii determined by this procedure for the atoms in the various models used are given in Table 3.2. The basis set for all models included Al 3*s*, 3*p* and 3*d* orbitals and Zr 4*s* and 4*d* orbitals.

The **k**-space integrations to determine the self-consistent charge density, density of states and crystal Hamiltonian orbital populations (COHP) were performed by the

tetrahedron method using 64 **k**-points in the irreducible wedge of the tetragonal cell for both the Zr_3Al_2 and U_3Si_2 structures.

Results and Discussion

The total energies for each of the eight models were calculated, and are reported in Table 3.3. Model 4 has the lowest energy, and was used as the reference point. The model with the highest energy is Model 3, at 7.72 eV, where the Al atoms occupy the real, distorted positions and the Zr arrangement is still idealized. This points to a coupling between the motion of the Zr and Al atoms in the *ab* plane, since Model 2B, where Al is only displaced in the *ab* plane, has the smallest energy difference, 0.36 eV, with Model 4, the real structure. As soon as Al is displaced along *c* or Zr is displaced in the *ab* plane, the energy of the structure increases rapidly, as seen in Model 2A (6.08 eV) and Model 5 (5.88 eV). But if these two displacements happen together, in the case of Model 6A, the resulting energy of the system is lowered significantly to 2.11 eV.

The band structures for each model were calculated, and they reveal a Peierls-type mechanism for the distortion that occurs. This is most pronounced along the $\Gamma \rightarrow Z$ direction of the Brillouin zone. In the band structure of Model 1 (see Figure 3.3), four bands converge near E_F at Z (0, 0, π/c). A similar convergence of bands also occurs for Model 4 at Z, but the four-fold degeneracy is clearly broken (see Figure 3.4). This suggests that degeneracies are lifted in the transition from the U_3Si_2 structure to the Zr_3Al_2 structure as the 3^2434 nets of Zr and Al distort. Analysis of the character of the bands present in each band structure verify this, as there is a splitting that occurs since the distortion of the Zr nets that causes the *d* orbitals of Zr to lose the degeneracy that is present in the U_3Si_2 structure, in particular the d_{yz} and the d_z^2 orbitals.

The density of states (DOS) curves were calculated for all models, and several interesting features can be noted on comparison of the transformations associated with Scheme I and Scheme II, and also on comparison of the benchmark models themselves (see Figures 3.5 and 3.6). For the case of Model 1, the Fermi energy lies on the shoulder of a collection of high-density states resulting from Zr 4*d* orbitals. This Fermi level is near a local minimum. Approximately 1.0 eV higher in energy there is a pseudo-gap in the DOS for Model 1. The DOS plot for Model 4 shows similar features. The Fermi level for this structure also lies on the shoulder of a collection of high-density states, again resulting from the Zr 4*d* orbitals. Also, a pseudo-gap appears in the DOS for this structure, in this case at ~1.5 eV higher in energy.

Summary

A series of models were constructed to make comparisons between the U_3Si_2 and Zr_3Al_2 structures, using Zr and Al as the building blocks. The starting point for these models was the U_3Si_2 structure, and models were created to simulate the transition from the idealized U_3Si_2 structure to the distorted Zr_3Al_2 structure. These models were used as the basis for TB-LMTO calculations to attempt to understand how these two structures are related. Analysis of the band structures of the models has shown that the transition from the U_3Si_2 structure to the Zr_3Al_2 structure lifts degeneracies along the $\Gamma \rightarrow Z$ direction, indicating a Peierls-type mechanism for the displacement occurring in the positions of the Zr atoms.

References

[1] R. Pöttgen, et al. *Z. Naturforsch.* **1994**, 49b, 1525.

[2] R. Pöttgen, et al. *Z. Naturforsch.* **1994**, 49b, 1309.

[3] F. Hulliger, et al. *J. Alloys Comp.* **1996**, 232, 160.

[4] M. N. Peron, et al. *J. Alloys Comp.* **1993**, 201, 203.

[5] P. Estrela, et al. *J. Phys: Cond. Mat.* **1998**, 10, 9465.

[6] R. Pöttgen and R. Dronskowski. *J. Solid State Chem.* **1997**,128, 289.

Table 3.1 Atomic Coordinates (x, y, z) for Models

Model 1

Al	0.389	0.389	0.25
Zr1	0.0	0.5	0.25
Zr2	0.181	0.181	0.0
Zr3	0.181	0.181	0.5

Model 2A

Al	0.389	0.389	0.21
Zr1	0.0	0.5	0.25
Zr2	0.181	0.181	0.0
Zr3	0.181	0.181	0.5

Model 2B

Al	0.625	0.625	0.25
Zr1	0.0	0.5	0.25
Zr2	0.181	0.181	0.0
Zr3	0.181	0.181	0.5

Model 3

Al	0.625	0.625	0.21
Zr1	0.0	0.5	0.25
Zr2	0.181	0.181	0.0
Zr3	0.181	0.181	0.5

Model 4

Al	0.125	0.125	0.21
Zr1	0.0	0.5	0.25
Zr2	0.34	0.34	0.0
Zr3	0.2	0.8	0.0

Model 5

Al	0.111	0.111	0.25
Zr1	0.0	0.5	0.25
Zr2	0.34	0.34	0.0
Zr3	0.2	0.8	0.0

Model 6A

Al	0.111	0.111	0.21
Zr1	0.0	0.5	0.25
Zr2	0.34	0.34	0.0
Zr3	0.2	0.8	0.0

Model 6B

Al	0.125	0.125	0.25
Zr1	0.0	0.5	0.25
Zr2	0.34	0.34	0.0
Zr3	0.2	0.8	0.0

Table 3.2 Wigner-Seitz Radii for Atoms

Model 1:		Model 4:	
Al	2.8100	Al1	2.5781
Zr1	3.7857	Al2	2.5781
Zr2	3.1699	Zr1	3.6904
Zr3	3.2262	Zr2	3.6904
		Zr3	3.4136
Model 2A:		Model 5:	
Al	2.6368	Al	2.6274
Zr1	3.8214	Zr1	3.7564
Zr2	3.4872	Zr2	2.9792
Zr3	2.9880	Zr3	3.4782
ES	1.7280	ES	1.8452
Model 2B:		Model 6A:	
Al	2.5599	Al	2.8052
Zr1	3.6041	Zr1	3.7939
Zr2	3.5743	Zr2	3.1523
Zr3	3.3637	Zr3	3.1641
		ES	1.3244
Model 3:		Model 6B:	
Al	2.6175	Al	2.6239
Zr1	3.8233	Zr1	3.8327
Zr2	3.3578	Zr2	3.2532
Zr3	3.2545	Zr3	3.3390

Table 3.3 Total Energies of Models (relative to Model 4)

Model 1	2.02 eV
Model 2A	6.08 eV
Model 2B	0.36 eV
Model 3	7.72 eV
Model 4 (observed)	0.00 eV
Model 5	5.88 eV
Model 6A	2.11 eV
Model 6B	6.93 eV

Scheme I

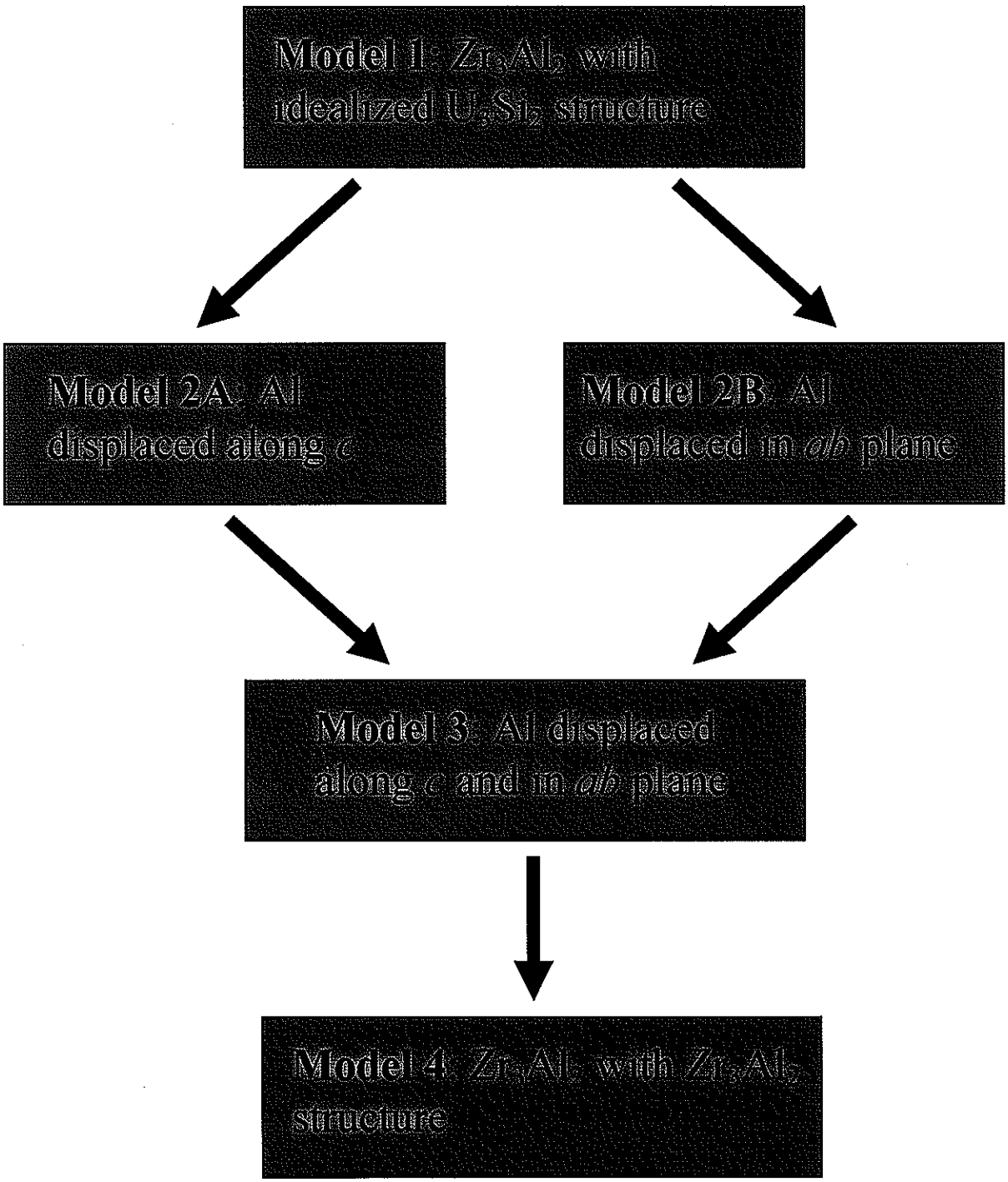

Figure 3.1 A diagram of Scheme I.

Scheme II

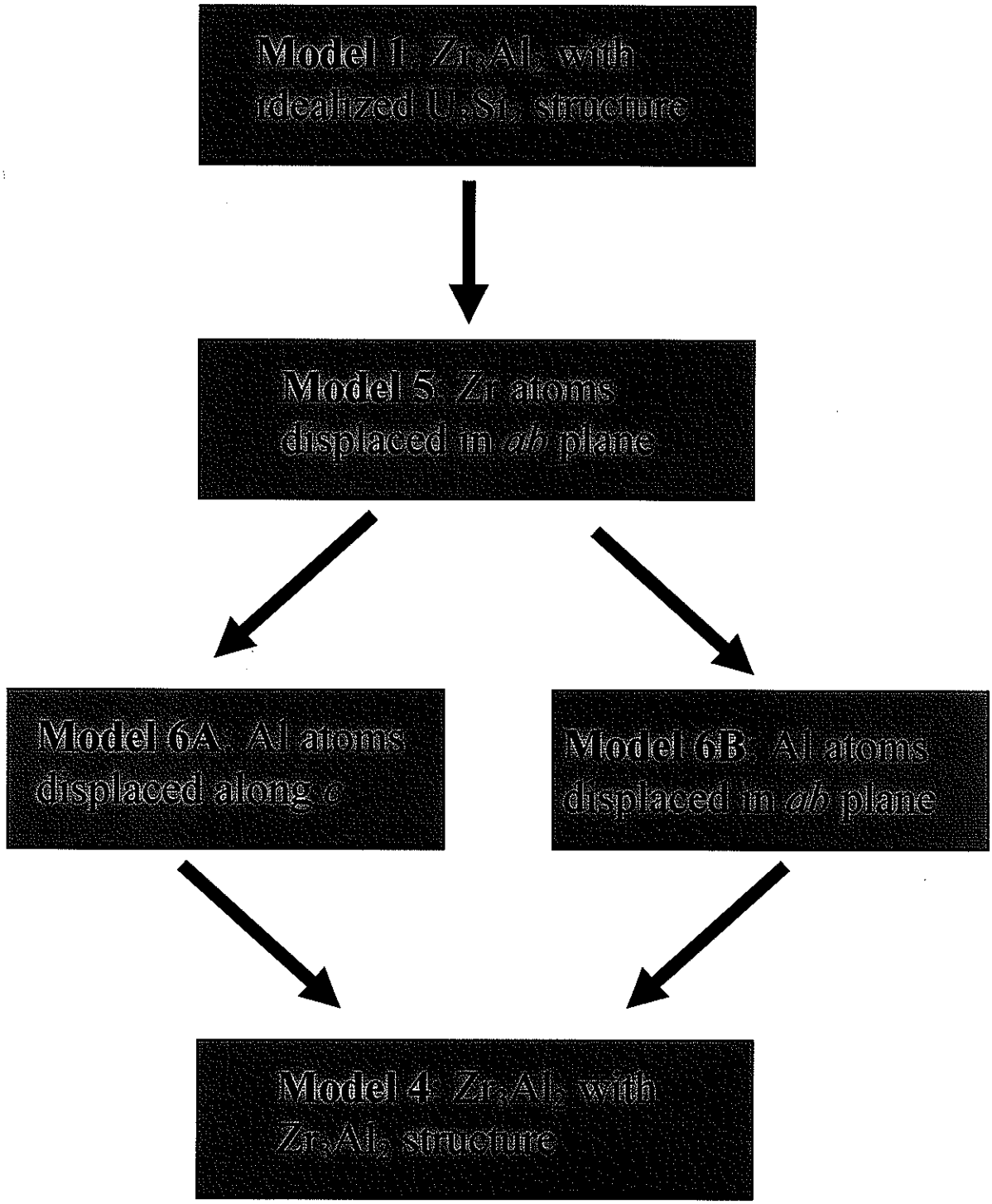

Figure 3.2 A diagram of Scheme II.

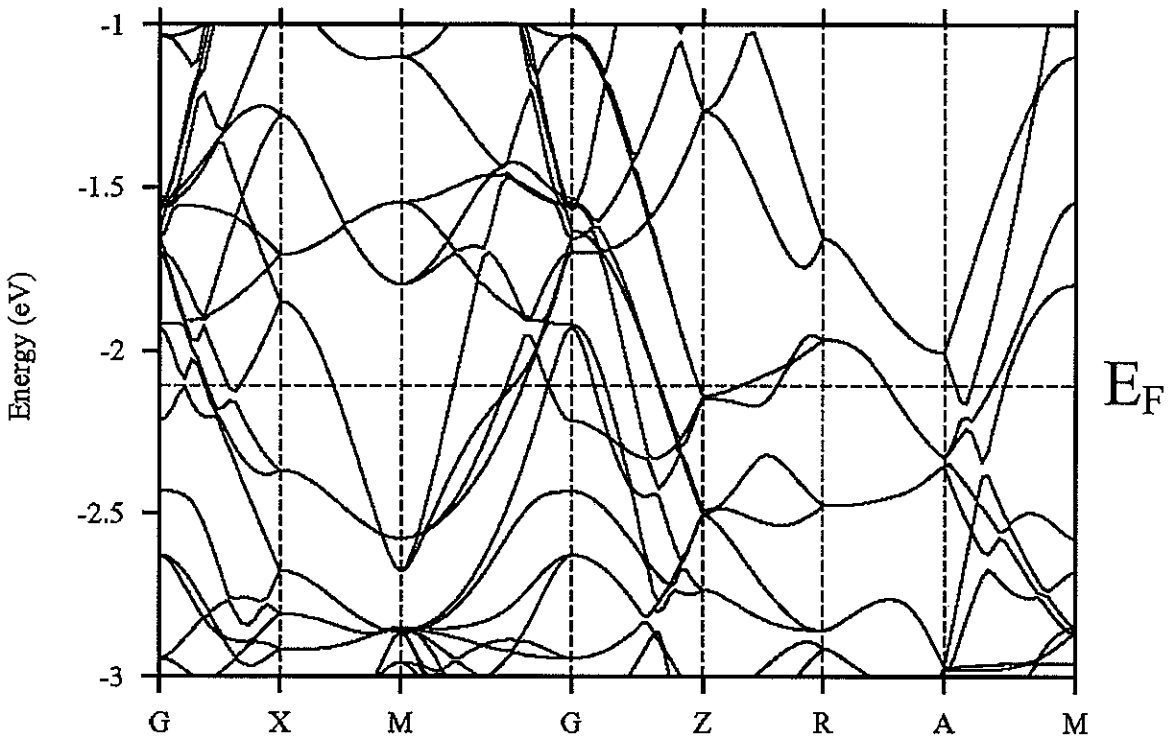

Figure 3.3 The band structure of Model 1, Zr_3Al_2 with the U_3Si_2 structure.

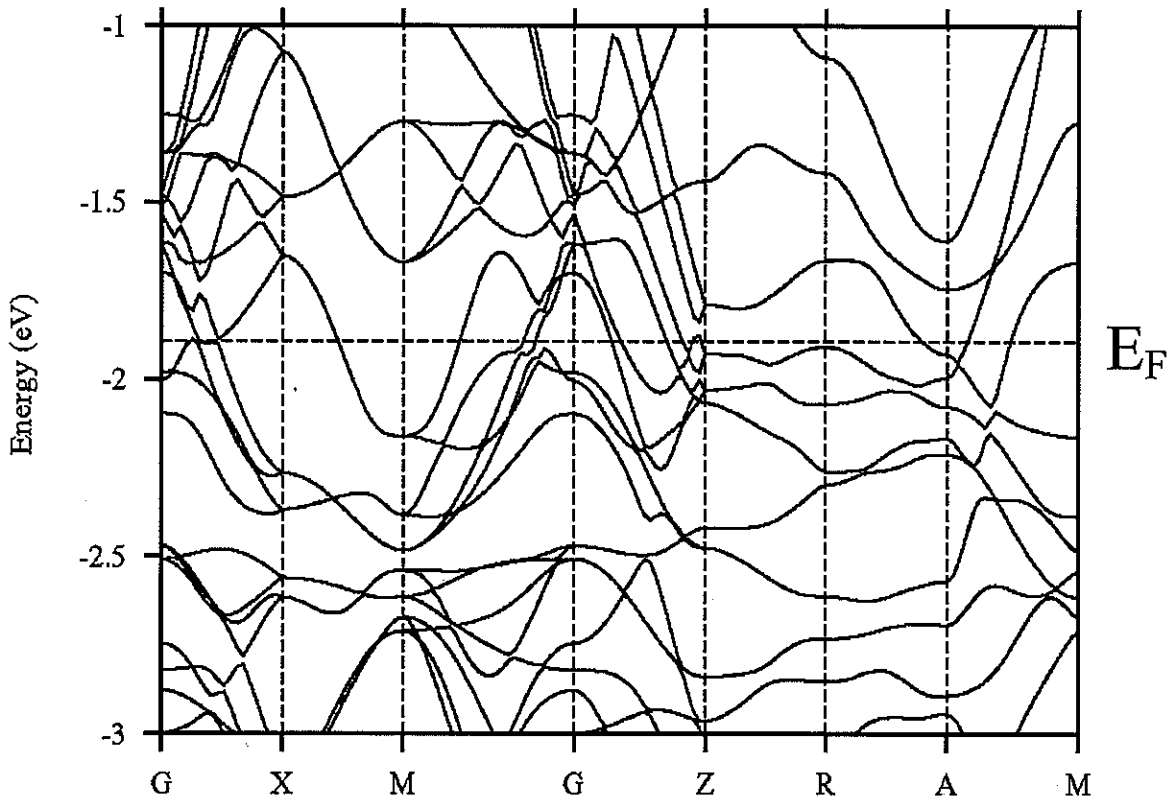

Figure 3.4 The band structure of Model 4, Zr_3Al_2 with the Zr_3Al_2 structure.

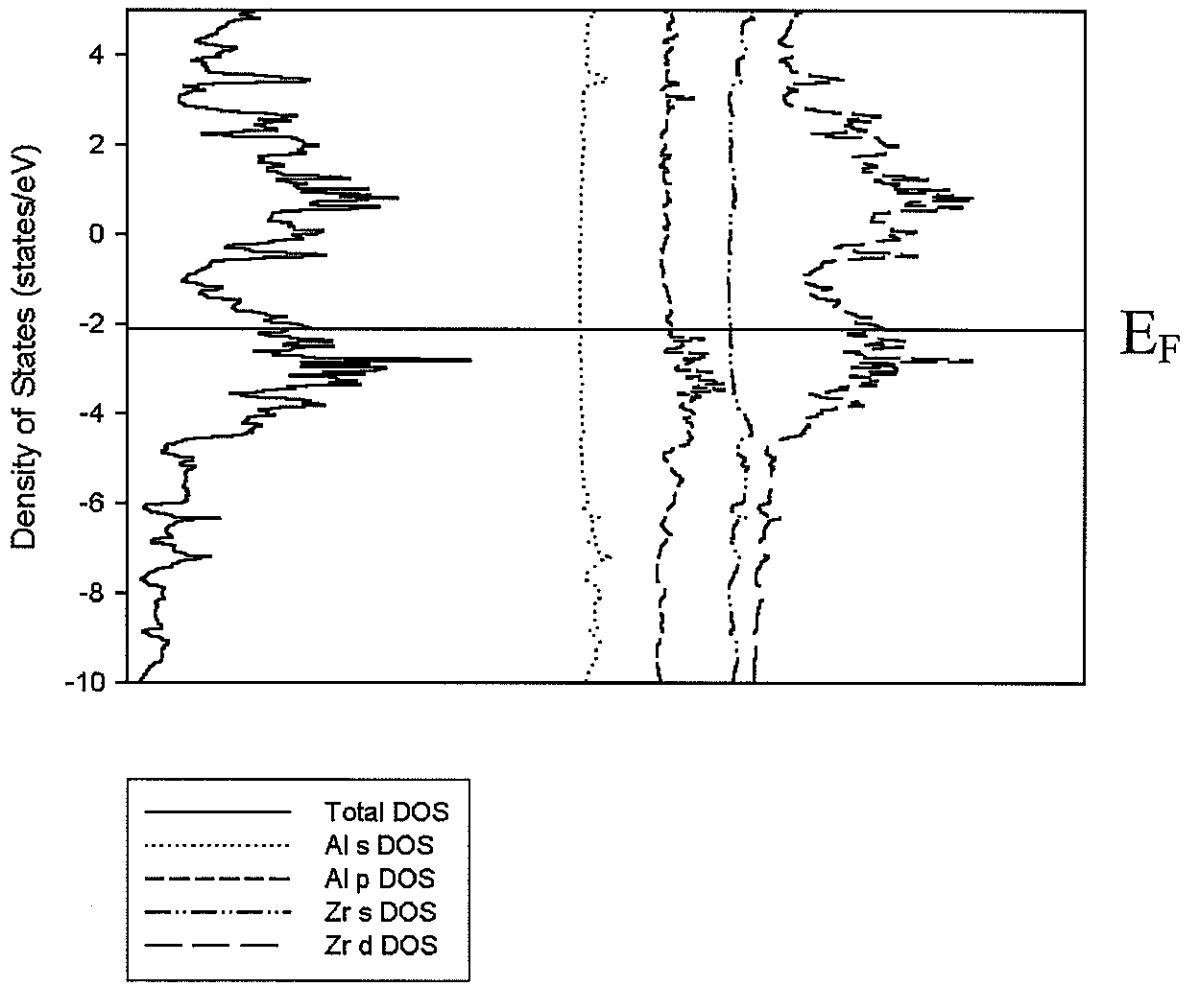

Figure 3.5 Density of states plot for Model 1.

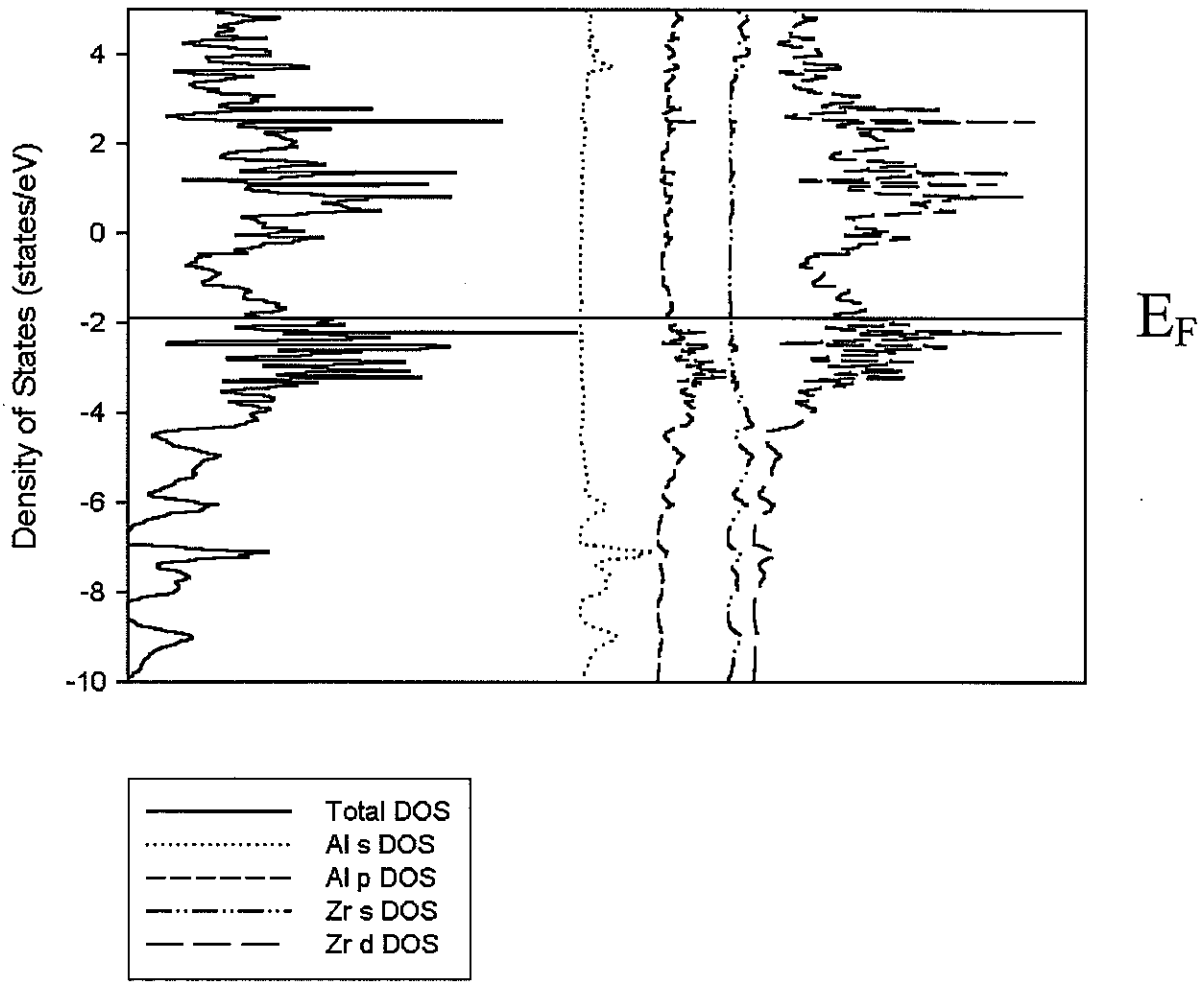

Figure 3.6 Density of states plot for Model 4.

Acknowledgements

I wish to acknowledge my gratitude to Gordie, for his limitless patience, understanding and encouragement, without which I never could have completed this work. I also appreciate the guidance that I received from the other members of my committee: John D. Corbett and Vitalij Pecharsky. I would like to thank my colleagues in the Miller group for their support as well: Wonyoung Choe, Olivier Gourdon, Delphine Gout, Mi-Kyung Han, Cathie Condron, Evan Benbow, Hyunjin Ko, Yurij Mozharivsky and Viken Djerdjian.

I am grateful to Greg Rice, Brian Trewyn and Kale Swainston for their friendship, and their efforts to help me maintain my sanity. Similar thanks go to the staff at KURE 88.5 FM, for allowing me to have an outlet to express myself outside of chemistry. Finally, I thank my family for their love.

This work was supported by the NSF and the DOE Complex Phenomena Initiative.